Characterization of CdZnTe semiconductor for applications in advanced computed tomography

By

PAVLO KARASYUK

Master of Science in Physics

Lakehead University

Thunder Bay, Ontario

2017

Characterization of CdZnTe semiconductor for applications in advanced computed tomography

Master of Science, 2017

Pavlo Karasyuk

Department of Physics

Lakehead University

Abstract

Cadmium zinc telluride (CdZnTe) is currently the only single crystalline semiconductor used in direct conversion gamma-cameras since CdZnTe can operate at room temperature, unlike other materials (e.g., germanium) that require liquid nitrogen cooling. Currently, CdZnTe-based single photon emission computed tomography (SPECT) cameras are successfully used in oncology and cardiology where they demonstrate diagnostic capabilities not achievable with indirect conversion SPECT technology.

The extremely high energy resolution of CdZnTe is very promising for other spectroscopy applications including spectral CT (Computed Tomography). It has been shown that use of CdZnTe detectors in CT systems has the potential to improve image quality and diagnostic capabilities while reducing the radiation dose to a patient for a wide range of imaging tasks. However, state-of-the-art CT imaging systems operate at much larger x-ray flux rates than used in gamma cameras (up to 100 Mcps/mm^2 in CT vs. 20-40 kcps/mm^2 in nuclear medicine systems). High flux rate operation puts a stringent requirement on detector properties like electron and hole drift mobilities and uniformity of the internal electric field.

Here we provide the detailed analysis of the charge transport properties of CdZnTe using time-of-flight (TOF), charge extraction by linearly increasing voltage (CELIV) and pulse height spectroscopy (PHS) methods. We show that electrons are much faster carriers in CdZnTe propagating through the material with drift mobilities around 1000 cm^{2}V^{-1}s^{-1} at room temperature (RT). Holes mobilities appear to be much smaller (around 60 cm^{2}V^{-1}s^{-1}). Evaluation of the temperature dependence of the carrier

mobilities shows that electron transport is affected by multiple scattering mechanisms while holes experience a trap-controlled transport mechanism. Our results suggest that the intrinsic electric field in our samples is affected by the presence of space charge which is distributed inhomogeneously throughout the sample thickness, showing two well-defined regions with different space charge concentrations. We extend the TOF theory to account for the influence of space charge distribution on the main electrodynamic parameters such as electric potential and intrinsic electric field. Although applied and tested here for a sample with two distinct regions of space charge accumulation, our theory can be used for practically any space charge distribution and the resulting field inhomogeneity.

Acknowledgements

I would like to express my deep sense of gratitude to my supervisor, Prof. Alla Reznik for the loyal guidance and help in the research work throughout my Master's study in Department of Physics at Lakehead University. Her invaluable advice and support always inspired me to new achievements. It would not be possible to complete this work without her painstaking efforts and diligent care.

I would like to thank my supervisory committee members, Prof. Apichart Linhananta and Prof. Mark Gallagher for teaching me physics and for their encouragement and advice.

My sincere thanks to all Reznik's research group for co-operation, selfless support, warm working atmosphere and helpful discussions on medical imaging applications.

My special thanks to Oleksandr Bubon, Sergey Reznik and Giovanni DeCrescenzo for the help with experiments and useful and interesting discussions on the results.

I am also grateful to Ira Blevis from Philips Healthcare for the opportunity to work in cooperation and providing us with material for research.

Many thanks to all my friends who shared moments of happiness and sadness with me during my research work.

Last but not least, I am infinitely grateful to my family Georgii, Olga, Valeriy Karasyuk and Boris Ievtukh for their love, support, care and endless patience.

Table of Contents

List of Figures

List of Tables

List of Acronyms

CdZnTe	Cadmium Zinc Telluride
FCC	Face-centered cubic
APF	Atomic packaging factor
THM	Travelling heater method
HPB	High-Pressure Bridgman
TOF	Time of flight
DC	Direct current
TFT	Thin Film Transistor
FWHM	Full Width Half Maximum
HEFT	High Energy Focusing Telescope
SPRD	Spectroscopic Personal Radiation Detector
PRD	Personal Radiation Detector
EHP	Electron hole pairs
PMT	Photomultiplier Tube
CT	Computed Tomography
HU	Hounsfield Units
PCCT	Photon-counting Computed Tomography
CELIV	Charge Extraction by Linearly Increasing Voltage
RC	Resistor-capacitor
PHS	Pulse Height Spectroscopy
MCA	Multi-channel Analyzer
CCE	Charge Collection Efficiency

1. Chapter 1: Growth techniques and fundamental properties of CdZnTe

1.1 Crystal structure

Cadmium zinc telluride, is a compound of cadmium telluride and zinc telluride. CdZnTe consists of two interpenetrating face-centered cubic (FCC) sub-lattices which are displaced from each other by one-quarter of a unit cell body diagonal shown in Fig. 1.1. Te occupies one sub-lattice while Cd and Zn occupy another sub-lattice. Typically, the CdZn sub-lattice in the CdZnTe crystal contains around 80-90% Cd atoms and around 10-20% Zn atoms. Such arrangement of atoms corresponds to a zinc blende crystal structure (diamond cubic crystal structure) [1].

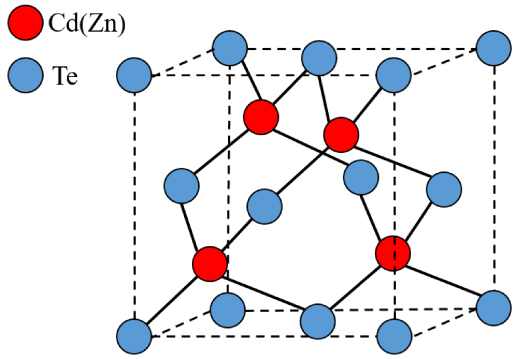

Figure 1.1. CdZnTe crystal structure and atomic arrangement in lattice. The red circles represent Cd (or Zn) atoms, the blue circles are Te atoms.

The atoms are bonded covalently in CdZnTe which is typical for zinc blende structured semiconductors. The space group of the zincblende structure is called $F\bar{4}3m$ with a two atom basis at (0,0,0) and (¼, ¼, ¼) as shown in Fig. 1.2.

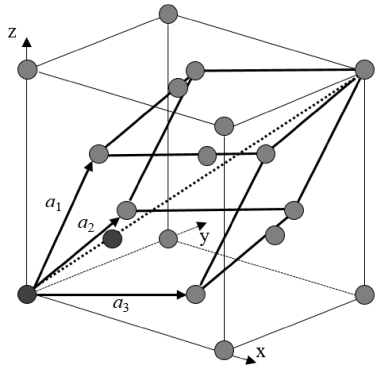

Figure 1.2. The primitive basis vectors of the face centered cubic (fcc) lattice and the two atoms forming the basis are highlighted [2].

The lattice constant of CdTe is 6.482 Å while the lattice constant for ZnTe is 6.104 Å [3]. The CdZnTe lattice constant can be estimated, using Vergard's Law, using the ratio of Cd to Zn atoms in the sample under study. For example, $Cd_{0.9}Zn_{0.1}Te$ has an estimated lattice constant of 6.444 Å while $Cd_{0.8}Zn_{0.2}Te$ has an estimated lattice constant of 6.406 Å. This shows that CdZnTe crystals have a lattice constant that shrinks as more zinc is added to the crystal.

1.2 Band structure

CdTe [1] and ZnTe [4] are direct band gap semiconductors which makes these compounds attractive for optical applications. The band gap of CdTe is equal to 1.44 – 1.5 eV [5, 6] while the bandgap of ZnTe is about 2.2 eV [7, 8]. At the same time, the band gap of CdZnTe is 1.52 – 1.57 eV while stoichiometry ranges from $Cd_{0.8}Zn_{0.2}Te$ to $Cd_{0.9}Zn_{0.1}Te$ [5, 9]. The theoretical band structure of ZnTe and CdTe obtained with the pseudopotential method are shown in Fig. 1.3 and 1.4 respectively [10].

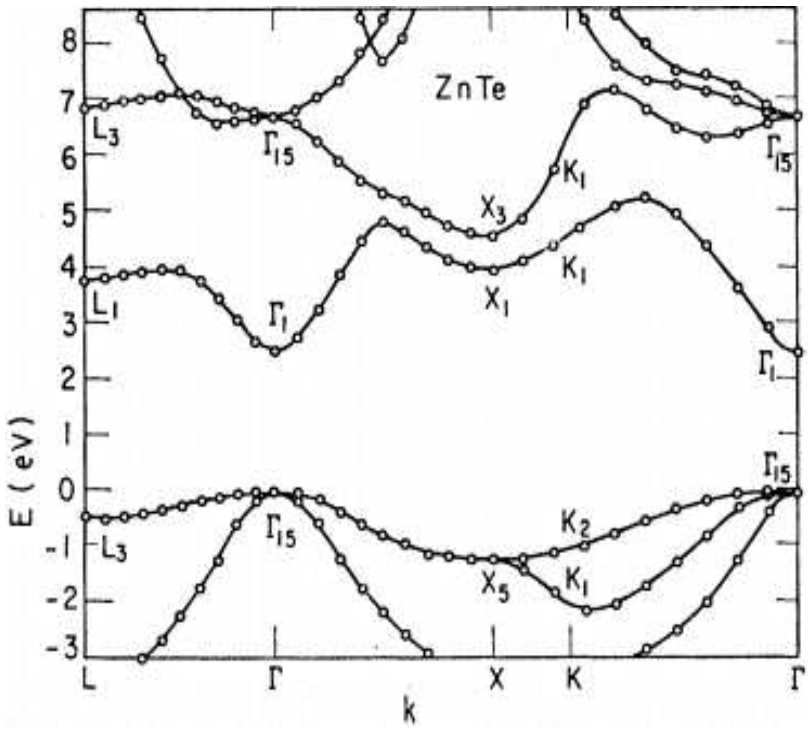

Figure 1.3. Band structure of ZnTe [10].

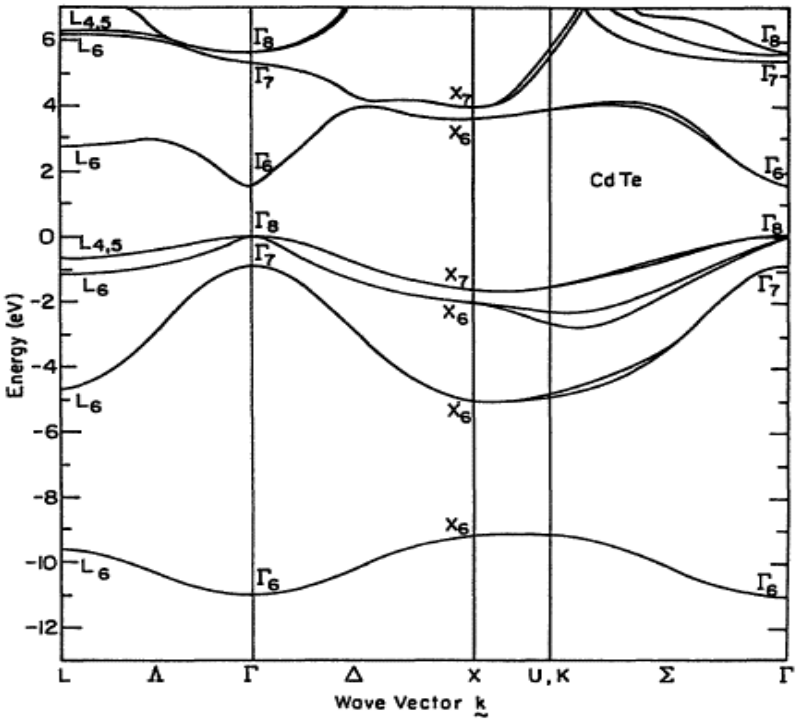

Figure 1.4. Band structure of CdTe [8].

From the energy band curvature, the effective masses of holes and electrons can be expressed as:

$$\frac{1}{m^*} = \frac{(2\pi)^2}{h^2}\frac{\partial^2 E}{\partial k^2} \tag{1.1}$$

The effective mass of electrons in CdZnTe is relatively low (~$0.11\ m_0$), offering good carrier transport properties. In CdZnTe (like in CdTe shown in Fig. 1.4), the top of each valence band curve is flatter than the steep curvature of the conduction band. Using equation (1.1) and plotting the second derivative of the energy band leads to larger effective masses for holes than for electrons. Effective masses in CdZnTe derived by different authors either theoretically *(theor)* or experimentally *(exp)* are shown in Table 1.1.

Table 1.1 Effective masses of electrons and hole in cadmium zinc telluride

Material	Electrons	Holes	Source
CdZnTe	$0.112\ m_0$	$0.8\ m_0$	Suzuki K et al. *(theor)* [11]

	$0.11\ m_0$	$0.73\ m_0$	Prokesch M. and Szeles C. *(exp)* [12]
	$0.112\ m_0$	$0.69\ m_0$	Suzuki K et al. *(theor)* [13]
	$0.11\ m_0$	$0.35\ m_0$	Kosyachenko L. et al. *(theor)* [14]
	$0.1\ m_0$		Bolotnikov A. et al. *(theor)* [15]
	$0.11\ m_0$		Macdonald R. et al. *(exp)* [16]
	$0.1\ m_0$	$0.81\ m_0$	Egan C. et al. *(theor)* [17]
	$0.088\ m_0$		Reno J. L. and Jones E. D. *(theor)* [18]

1.3 Crystal growth techniques

Over the years, various crystal growth methods have evolved to produce a CdZnTe crystal with good physical and electro-optical properties. The quality of the as–grown crystal depends on the number of structural defects formed during growth such as pipes, cracks, grain boundaries, twins, precipitates and inclusions [19]. Despite years of technological effort, the yield of high quality (low defect concentration) CdZnTe crystals is very low, and it is still very challenging and expensive to produce high purity, large single crystals.

Most frequently, CdZnTe crystals are produced by melt-growth methods such as the Bridgman, High-Pressure Bridgman (HPB) [20, 21, 22], and the Traveling Heater methods (THM) [23, 24]. A brief review of the growth techniques is given below.

1) Bridgman method

The main idea of the Bridgman method is to grow single-crystalline CdZnTe using cadmium (Cd), tellurium (Te) and zinc (Zn) ingots weighed to stoichiometric proportions. Prior to being mixed in the crucible, multiple purification such as etching in dilute nitric acid to remove the surface contamination are done with the precursor materials. Since refined ingots are prone to the formation of oxides, it is recommended to avoid any exposure to air during storage. The formation of oxides is a significant problem since as the temperature rises, oxygen begins to evaporate and thereby affect the crystallinity and purity of the resultant material. The material of choice for a crucible is porous graphite which facilitates the escape of gases (like oxygen) from the growing

material thus reducing the concentration of defects and impurities in the final crystal. The crucible is heated sequentially to the melting points of the constituent compounds, CdTe and ZnTe (~1100 °C), and then slowly cooled starting from the bottom end as shown in Fig. 1.5. At the melting point of the substance, both solid and liquid forms of the material will be present, and as the crucible moves across the temperature gradient, infinitesimal layers of the melt continue to cool, solidify, and form the crystal. The furnace can be vertical or horizontal which makes it possible to run the process in both geometric orientations. Ultimately, a single-crystal material is gradually formed along the length of the container.

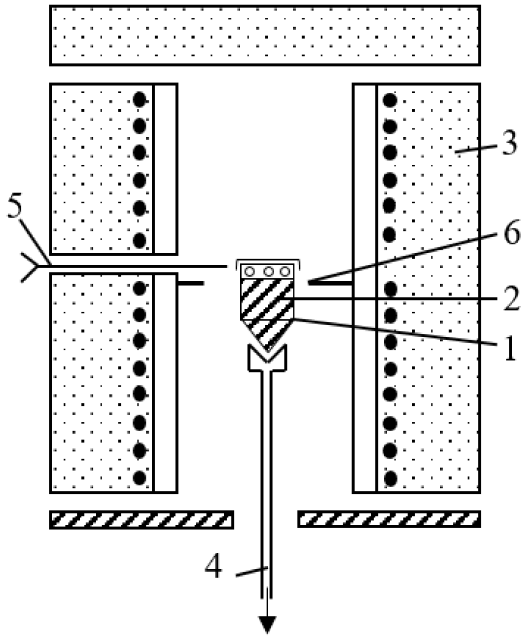

Figure 1.5. The schematic of the apparatus for growing CdZnTe crystals by the Bridgman method. 1 – a crucible with the melt, 2 – mix of Cd, Zn and Te, 3 - furnace, 4 - refrigerant, 5 -thermocouple, 6 - heat shield.

The Bridgman method is a basic growth technique with a growth rate of ~1 mm/hr. Since the CdZnTe melt consists of volatile components, the disadvantage of this method is an excess of Cd-vacancies due to cadmium diffusion out of the crucible during the growth. Cd-vacancies act as acceptors degrading the electronic properties of the CdZnTe. In addition, the resulting crystal usually contains an excess of tellurium atoms that leads to the formation of dislocations and grain boundaries (Te-precipitates). The trapping centres

created by Cd-vacancies or Te-precipitates in the CdZnTe can be reduced (or passivated) by adding additional cadmium or doping with elements such as In or Al. The final CdZnTe crystals, often produced as comparatively small ingots of the material, are tiled together to make a large detector and increase the detection area. The CdZnTe crystals produced by the Bridgman technique have slightly lower electron and hole lifetimes and sufficiently high resistivity (about 10^9 Ωcm [25, 26]) in contrast to other methods.

2) High-Pressure Bridgman method

The High-Pressure Bridgman method is one of the modified Bridgman methods used for crystal growth. In the HPB method the conventional Bridgman furnace is housed in a specially designed chamber to apply an external high pressure of inert gas (argon, 10-150 Atm) to the crucible during the crystal growth as shown in Fig. 1.6.

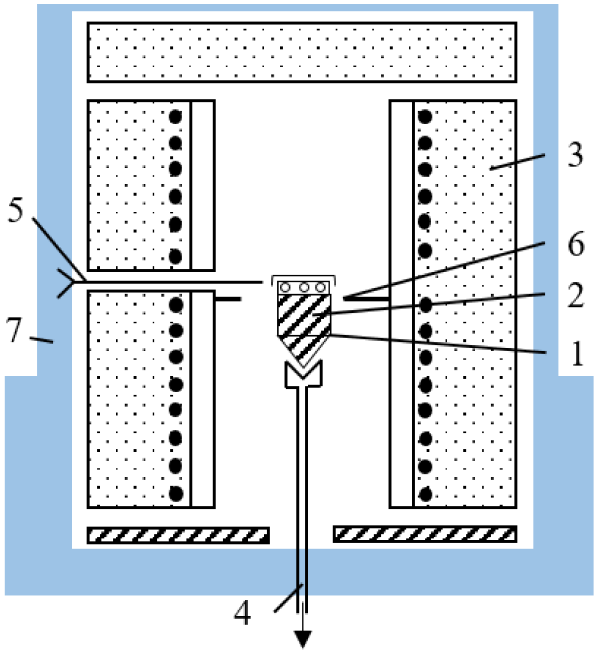

Figure 1.6. The schematic of the apparatus for growing CdZnTe crystals by the High-Pressure Bridgman method. 1 – a crucible with the melt, 2 – mix of Cd, Zn and Te, 3 – furnace, 4 – refrigerant, 5 – thermocouple, 6 – heat shield, 7 – high-pressure chamber.

An advantage of the HPB method is that the high pressure reduces the probability of Cd loss through evaporation. Despite the fact that the high pressure inhibits the evaporation of cadmium, some losses are still present. The complete cycle of crystal growth is about 3-4 weeks with growth rates of ~1mm/hr. The final crystals have shown very promising electronic properties mostly due to a lower concentration of Cd-

vacancies. The typical resistivity of CdZnTe grown by the HPB is about $10^{10}\Omega$cm, and the mobility-lifetime products ($\mu\tau$) are about 10^{-3} cm^2V^{-1} and 10^{-5} cm^2V^{-1} for electrons and holes, respectively. Unfortunately, the presence of defects like cracking, pipes or twins significantly reduces the amount of useful material to 25% [22]. The HPB method is widely used by one of the largest suppliers of CdZnTe crystals, the eV Products company [27].

3) Traveling Heater Method

The Traveling Heater growth technique of CdZnTe crystals is shown in Fig. 1.7.

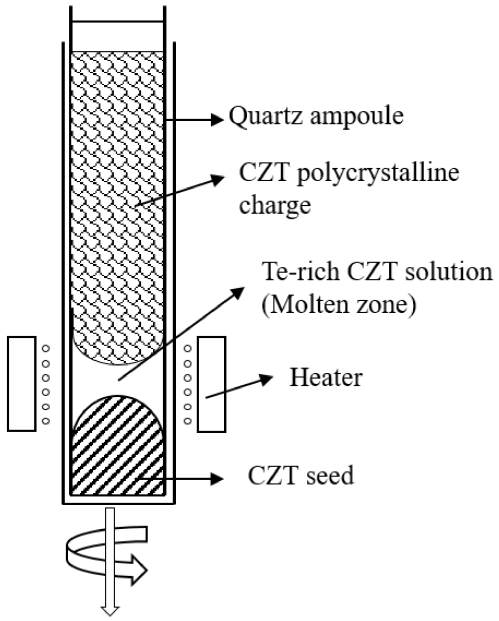

Figure 1.7. A schematic of the apparatus for growing CdZnTe crystals by the THM [28].

The THM is a seeded growth process that runs by the precipitation of grown material from solution. In THM, a high-purity quartz ampoule is typically used as a growth container instead of a graphite crucible to reduce contamination from the container. The ampoule is usually coated with carbon to avoid sticking or a reaction between the charge and the container. The upper part of the ampoule is occupied by the polycrystalline CdZnTe (or a stoichiometric alloy of Cd, Zn and Te) while a pure Te ingot (or powder) and a CdZnTe seed crystal occupies the middle and bottom parts, respectively. The polycrystalline CdZnTe ingots used in THM are previously synthesized and grown in a separate module. The seed CdZnTe crystal is a crystal with known

orientation and pre-synthesized in stoichiometric proportions using another method of growth (like HPB). At the beginning of the process, the pure tellurium is melted creating a molten zone. During the vertical growth process, either the ampoule or the heater can be moved to produce a molten zone. For the growth process to occur evenly, the ampoule rotates clockwise and anti-clockwise periodically. As the heater moves, the bottom layer of the polycrystalline CdZnTe dissolves into the molten zone, and at the same time the bottom layer of the molten zone cools and deposits crystalline CdZnTe onto the top of the seed crystal. One of the main differences between the THM and the Bridgman methods is the fact that growth occurs under much lower temperature conditions (~600 °C – 900 °C) offering a material with higher crystalline quality [28].

Currently, THM is the most promising method for the growth of high-purity, comparatively large volume CdZnTe materials for x-ray and gamma-ray detection. CdZnTe crystals produced by THM exhibit excellent electronic properties with high resistivity ($10^{10}\Omega$cm), and a good electron mobility-lifetime product (10^{-3} cm^2V^{-1}) [29, 30]. However, THM is a very time-consuming method of crystal growth, as the growth rate is about 3-5 mm/day in contrast to mm/h in other methods. The Traveling Heater Method is widely used by Redlen Technologies [29].

1.4 Transport properties

The transport properties were at the focus of much research in many groups due to the wide applicability of CdZnTe in x-ray and gamma-ray detection systems. Electron and hole mobilities, lifetimes, as well as their temperature and electric field dependence, were measured by a large variety of techniques with the major ones being time-of-flight (TOF) [31] and pulse height spectroscopy (PHS) [8].

The TOF technique was developed in the 1960s to investigate charge transport in photoconductors with a low concentration of equilibrium carriers and is illustrated in Fig. 1.8.

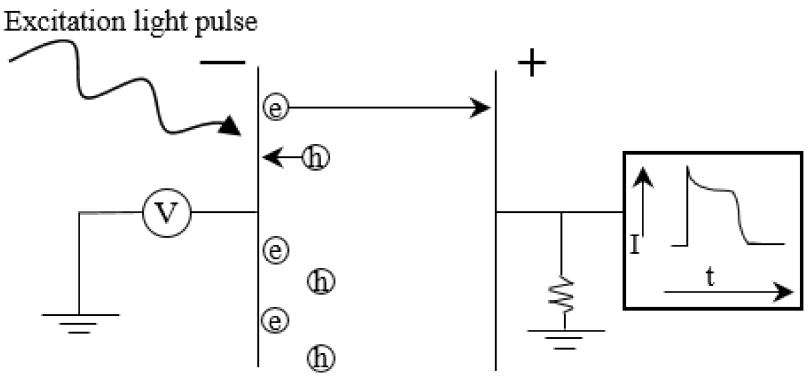

Figure 1.8. Schematic diagram of time-of-flight setup.

In the TOF method, carriers are generated near the electrode of the biased capacitor structure by a short pulse of highly absorbed light. The duration of the pulse should be much shorter than the drift time of carriers for accurate measurements. Mobile electrons and holes drift across the sample under the action of a high electric field to the oppositely charged electrode. As a result of carrier drift, a transient current pulse as a function of time is obtained and displayed on the oscilloscope. A distinctive feature of the TOF method is that the motion of both carrier types can be observed separately by either directing the highly absorbed light on one or the other contact, or by reversing the polarity of the applied voltage. The average carrier drift velocity can be calculated from the carrier transit time by:

$$\upsilon_d = \frac{d}{t_{transit}} \tag{1.2}$$

Using the carrier drift velocity, the mobility can be determined as:

$$\mu = \frac{\upsilon_d}{F} = \frac{d^2}{t_{transit} V} \tag{1.3}$$

where F is applied electric field, d is the sample thickness and $t_{transit}$ is the transit time of the carrier.

The time of flight technique is widely used to evaluate charge transport in different photoconductors especially high resistivity, wide bandgap materials used as optical sensors. An advantage of TOF is the ease of use, since the configuration of the contacts on most conventional detectors is ideally suited to this technique.

The pulse height spectroscopy is another method to characterize the transport properties of a material. In PHS the biased detector is exposed to x-ray or γ-ray radiation. Each absorbed high energy photon produces a charge pulse which is initially amplified by a preamplifier, which converts the charge into a voltage pulse. The preamplifier is usually connected via a BNC cable with a shaping amplifier. The output signal from the preamplifier is further filtered from the background noise and shaped by a shaping amplifier. The time that the shaping amplifier spends processing is known as the shaping time. After shaping, the output analog pulses (signals) from the amplifier are sent to a Multi-Channel Analyzer (MCA). The MCA digitizes the incoming signals into digital data and classifies the received pulses in a given range by height. The histogram, produced by the MCA, contains information about the pulse height (photon energy) on the x-axis while y-axis corresponds to the number of counts of radioactive photons interacting with the detector in a certain energy window. The final histogram is displayed on the computer screen. The complete pulse height analysis system is shown in Fig. 1.9.

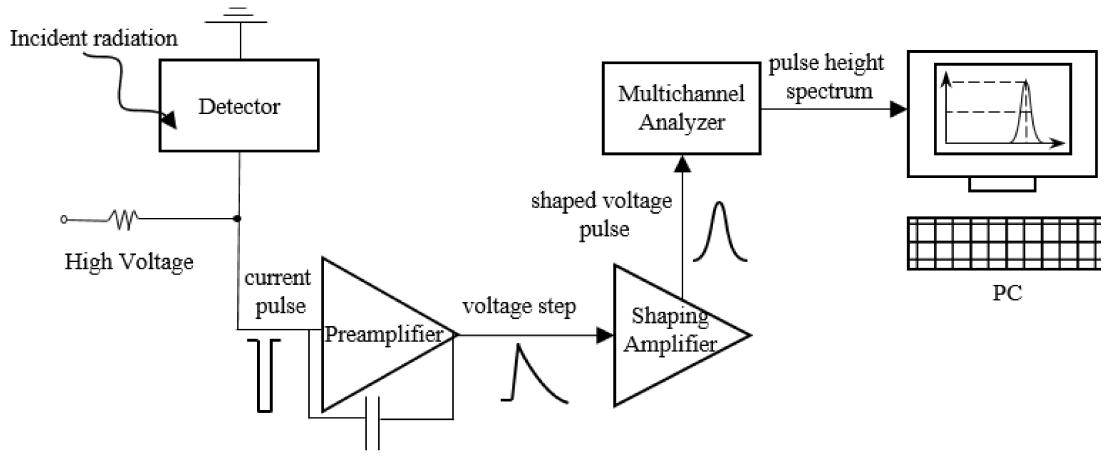

Figure 1.9. The schematic diagram of the complete system for pulse height analysis.

The mobility-lifetime product of a charge carrier is one of the major properties that affects the PHS spectrum shape which becomes asymmetrical if one type of x-ray generated carrier is trapped (or lost due to a short lifetime) and does not contribute to the collected charge [32]. The conventional method of determining the mobility-lifetime product value from the pulse height spectrum is based on the Hecht equation [33]. The equation describes the ratio of charge collected experimentally, Q_0, to the theoretical

value of the total carriers created by the x-ray absorption, Q. Such ratio is termed as charge collection efficiency and can be written as:

$$\eta = \frac{Q_0}{Q} = \frac{\lambda_e}{d}(1 - e^{-\frac{d-x_i}{\lambda_e}}) + \frac{\lambda_h}{d}(1 - e^{-\frac{x_i}{\lambda_h}}) \tag{1.4}$$

where x_i is the distance from the irradiated electrode to the position of the generated charge, $\lambda_{e,h} = \mu_{e,h}\tau_{e,h}F$ is the carrier mean free path (schubweg).

Since CdZnTe is a photoconductor, the majority of authors use alpha particles, low x-ray energy radiation or highly absorbed light to generate carriers on the anode or cathode side of the biased sample to investigate single (electrons or holes) charge carrier propagation through the bulk of the material. For example, at the early stages of CdZnTe technology development, Tousignant et al. [34] experimentally measured the effective electron and hole mobilities using alpha particle radiation on a sub-millimetre CdZnTe detector. The reported charge transport model used to calculate the mobilities was based on a multiple trapping-detrapping mechanism [35] given by:

$$\mu_{eff} = \mu_0 \frac{\tau_t}{(\tau_t + \tau_r)} \tag{1.5}$$

where μ_{eff} is the mobility due to a multiple-trapping mechanism, μ_0 is the microscopic mobility, τ_r is average time a hole localizes at the trap and τ_t is the time that the hole is free. The calculated effective mobilities were 690 $cm^2V^{-1}s^{-1}$ for electrons and 4.7 $cm^2V^{-1}s^{-1}$ for holes. Furthermore, the $\mu\tau$ product for holes was calculated and was found to be $2.8x10^{-5}$ cm^2V^{-1}. It was emphasized that most holes were trapped at deep traps before reaching the negatively charged electrode. Cho et al. [36] published findings on the carrier mobility of a CdZnTe crystal using a time-of-flight technique yielding an electron mobility value of 906.4 $cm^2V^{-1}s^{-1}$, much higher than that previously reported by Tousignant et al. The performance of thick CdZnTe detectors grown by vertical Bridgman (VB) and HPB techniques were evaluated using alpha particles and low energy x-rays by Veale et al. [37] Since the penetrating depth of the alpha particles in CdZnTe is ~18μm (for 5.5 MeV α particle) [38], the induced current was mainly created by one type of carrier. To obtain the $\mu\tau$ product the charge collection efficiency was plotted as a

function of applied electric field and fitted to the Hecht equation for single charge carrier transport [39] given by:

$$\eta = \frac{Q_0}{Q} = \frac{\lambda}{d}(1 - e^{\frac{d}{\lambda}}) \tag{1.6}$$

A mobility-lifetime product of 1.25×10^{-3} cm^2V^{-1} ± 0.02×10^{-3} cm^2V^{-1} and 1.92×10^{-3} cm^2V^{-1} ± 0.05×10^{-3} cm^2V^{-1} for electrons was estimated using VB and HPB methods, respectively. This result corresponds to electron mobilities of 1080 $cm^2V^{-1}s^{-1}$ ± 5 $cm^2V^{-1}s^{-1}$ and 1114 $cm^2V^{-1}s^{-1}$ ± 9 $cm^2V^{-1}s^{-1}$, respectively, demonstrating an improvement in transport properties with the HPB growth technique. Auricchio et al. [40] performed a similar analysis to Veale et al., calculating both the hole and electron mobility-lifetime products using alpha particle and gamma-ray spectroscopy. The hole mobility-lifetime product was found to be 1.1×10^{-5} cm^2V^{-1} ± 0.1×10^{-5} cm^2V^{-1}, smaller than the result by Tousignant et al. but still the same order of magnitude. The electron mobility-lifetime was found to be around 1.9×10^{-3} cm^2V^{-1} ± 0.1×10^{-3} cm^2V^{-1}, similar to those found by Veale et al.

Ruzin and Nemirovsky [38] used x- and gamma-ray pulse height spectroscopy analysis to determine both the hole and electron mobility-lifetimes for CdZnTe samples grown using Bridgeman and HPB techniques. Similar to the method reported by Cho et al. and Veale et al., the average charge collection efficiency was plotted as a function of applied bias. The mobility-lifetime products were found to be around 2×10^{-3} cm^2V^{-1} for electrons, and 1×10^{-5} cm^2V^{-1} for holes when CdZnTe was grown by the HPB technique. The electron mobility value was measured independently by the TOF technique and was found to be 1060 $cm^2V^{-1}s^{-1}$ which is comparable to the values published by Veale et al [37]. For the CdZnTe sample grown using the Bridgeman technique, the obtained mobility-lifetime values were slightly lower: 9×10^{-4} cm^2V^{-1} for electrons and 1×10^{-7} cm^2V^{-1} for holes. Chen et al. [29] also used x-ray and γ-ray spectroscopy to characterize CdZnTe samples grown by THM. A superior material purity was reported leading to an electron mobility-lifetime of $\mu\tau_e > 2 \times 10^{-2}$ cm^2V^{-1} which is higher than ever reported before.

Of particular interest is the ability to determine the mobility and other transport properties of a CdZnTe sample using optical TOF measurements. Suzuki et al. [11] used

a tunable nitrogen laser (λ = 337 nm) with 300 ps pulses at a repetition rate of 10 Hz to study the transport properties of a CdZnTe sample grown by the HPB technique. The benefit of using laser pulses as opposed to gamma-rays or x-rays (or even alpha particles) is the fact that the optical radiation only penetrates to a depth of ~1-2 μm into the CdZnTe sample, allowing one to assume that all the collected charge carriers were produced at the surface of the sample exclusively. To obtain the mobility values, Suzuki et al. plotted the drift velocity as a function of the electric field. Applying Eq. 1.3, the electron and hole mobility values were 960 $cm^2V^{-1}s^{-1}$ and 56 $cm^2V^{-1}s^{-1}$, respectively. The TOF technique was used to estimate the carrier's mobility-lifetime products by integrating the photocurrent transient over time for different applied fields. The mobility-lifetime products were found to be around $5x10^{-4}$ cm^2V^{-1} for electrons and $1.6x10^{-4}$ cm^2V^{-1} for holes meaning that the $\mu\tau$ product for holes were significantly improved in contrast to the previously reported values by Tousignant et al. and Ruzin et al. Furthermore, Suzuki et al. was one of the first to analyze the temperature dependence of the electron and hole mobilities to evaluate carrier transport mechanisms. Initial analysis was done under the assumption that several scattering mechanisms take part simultaneously, namely, optical phonon scattering, acoustic phonon scattering, ionized impurity scattering and alloy scattering. Since fitting the experimentally observed results with a combination of these scattering mechanisms did not yield a satisfactory result, Suzuki et al. introduced trap-controlled transport (Eq. 1.2) to account for the variation of mobility with temperature. Subsequently, Suzuki et al. stated that electron transport is mostly limited by scattering while the major transport mechanism for holes was multiple trapping [41, 1]. In addition, fitting the experimental results allowed derivation of important parameters like the ionized impurity concentration. The ionized impurity concentration has direct impact on the dark resistivity (or conductivity) and mobility of the semiconductor and was found to be comparatively high ($2.5x10^{17}$ cm^{-3}).

Suzuki et al. [42, 43] also investigated the effect of both pulsed bias and DC bias on CdZnTe transport. To study the bias dependence of the photocurrent transient waveforms, Suzuki et al. applied a voltage to the CdZnTe using a custom-made system that controlled the bias pulse duration (T_B) from 125 μs to tens of milliseconds. The laser excitation was performed with a specified delay (ΔT_L) after the bias pulse was applied.

This delay time was called 'suspension time' and varied from 30 μs to 37 ms ($\Delta T_L < T_B$). A schematic illustration of the timing between the laser pulse and application of a bias pulse used by Suzuki et al. is shown in Fig 1.10.

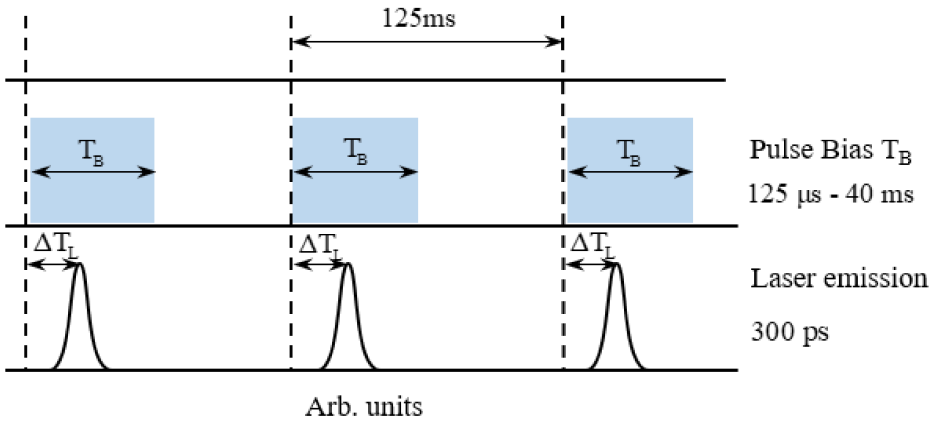

Figure 1.10. A schematic illustration of the timing between the laser pulse and application of bias pulse used in optical TOF technique [43].

Although the transit time of the carriers appeared to be the same in each case, a remarkable change in the transient current waveform under a DC bias compared with the pulsed bias was observed. Suzuki et al. explained this behaviour by an increase of the internal electric field towards the back of the CdZnTe sample under DC bias. Furthermore, a Monte Carlo simulation technique was used to estimate the space charge density (assuming a homogeneous distribution across the sample thickness) and found to be 1.2×10^{11} cm^{-3} for electrons and 3.1×10^{10} cm^{-3} for holes. The reason why the space charge density was higher in the case of hole transport was not explained. The CdZnTe transport properties derived from the publications analyzed above are summarized in Table 1.2.

Table 1.2 CdZnTe transport properties

Source	Growth method	μ_e [$cm^2V^{-1}s^{-1}$]	μ_h [$cm^2V^{-1}s^{-1}$]	$(\mu\tau)_e$ [cm^2V^{-1}]	$(\mu\tau)_h$ [cm^2V^{-1}]
Tousignant [34]	-	690	4.7 50		2.8×10^{-5}
Cho et al. [36]	-	906.4		9.8×10^{-3}	8.2×10^{-4}

Veale et al. [37]	VB, HPB	1080		$1.2x10^{-3}$	$5.8x10^{-5}$
Auricchio et al. [40]	VB			$1.9x10^{-3}$	$1.1x10^{-5}$
Ruzin et. al. [38]	VB, HPB	1060		$2x10^{-3}$ $9x10^{-4}$	$1x10^{-5}$ $1x10^{-7}$
Chen et al. [29]	THM			$1.3x10^{-2}$	
Suzuki et al. [11]	HPB	960	56	$5x10^{-4}$	$1.6x10^{-4}$

Overall, electrons are much faster (~14-17 times) carriers than holes in CdZnTe. Electrons experience trap-free transport that is mostly controlled by several scattering mechanisms (ionized and neutral impurity scattering, phonon scattering) while the main transport mechanism for holes in CdZnTe is multiple-trapping. It should be emphasized that charge transport properties strongly depend on the manufacturer, method of growth, doping and the concentration of various kinds of internal defects which create new energy levels inside the bandgap, and act as traps for holes or electrons. Advances in growth techniques allow CdZnTe crystals with higher mobility and $\mu\tau$ products; however, the yield of useful materials of large volume still leaves much to be desired. Based on the results demonstrated above, the best method to obtain a pure CdZnTe crystal with the least number of defects and satisfactory electrical properties is THM.

2. Chapter 2: Direct conversion CdZnTe radiation detectors and their applications in x-ray and gamma-ray detection

2.1 Principles of x-ray detection

Radiation detectors can use either a direct or indirect scheme of converting X-rays into electrical charge.

2.1.1 Indirect conversion detection

Indirect conversion detectors have a multiple step conversion process for x-ray detection. At the first conversion stage, the x-ray (or γ-ray) photons are absorbed within a scintillator material which is optically coupled to an array of optical sensors (either

photomultiplier tubes or solid state photosensors). The high energy x-ray photons are converted into photons in the visible or near visible range and emitted by the scintillator. The number of photons is proportional to the incident x-ray energy. The light emitted from the scintillator is converted into the electrical charge by an array of photosensors and further collected by the underlying readout electronics. There are two types of scintillators used in indirect conversion, namely, monolithic (unstructured) and structured as shown in Fig. 2.1.

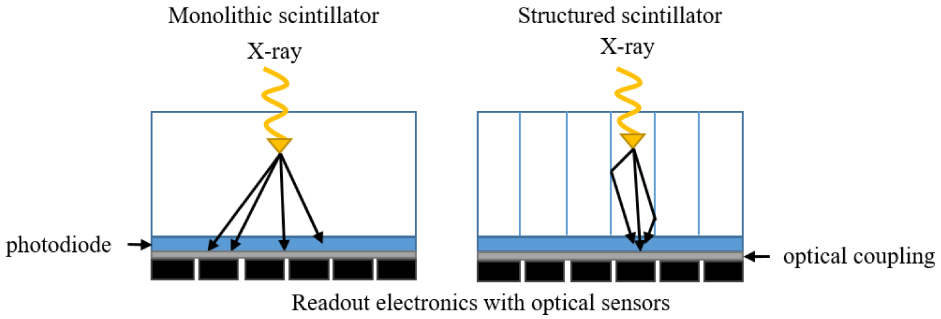

Figure 2.1. Structured and unstructured (monolithic) scintillators for indirect conversion detectors.

The most common monolithic scintillators are gadolinium oxysulfide (Gd_2O_2S) and sodium iodide (NaI). The advantage of monolithic scintillators is their low-cost, while significant drawbacks include the comparatively low light yield and the inability to control the dispersion of the emitted scintillation photons. The latter is of importance if each channel (pixel) of the readout electronics is read-out individually. In this case photon scattering to neighboring pixels reduces the spatial resolution of the detector. The adverse effect of the light dissipation on a spatial resolution is shown in Fig. 2.2.

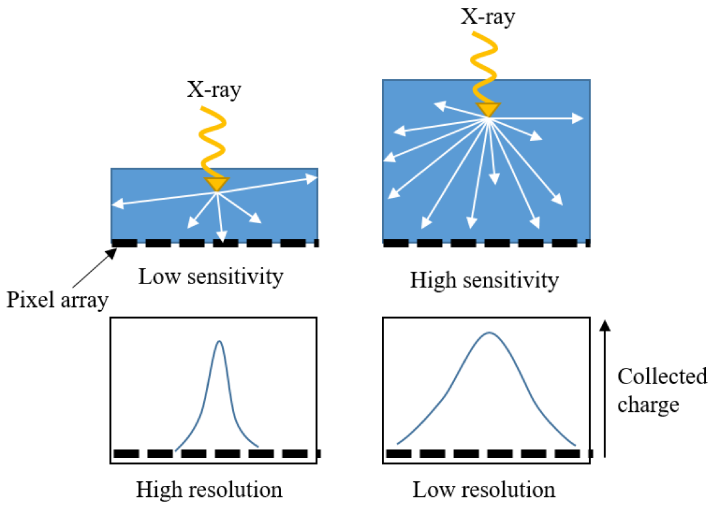

Figure 2.2. The effect of spreading the light in the scintillator on spatial resolution. The thicker the detector the better the absorption and the worse the resolution [44].

As can be seen from the Fig. 2.2, to achieve better spatial resolution, a thinner detector is needed. However, a thick detector is required to achieve proper absorption efficiency of the x-rays which leads to image blurring. Therefore, there is always a tradeoff between spatial resolution and sensitivity if an indirect detection scheme is used.

To improve the spatial resolution, a structured cesium iodide (CsI) scintillator was developed (Fig. 2.1, right). The benefit of the structured scintillators is a needle-like (approximately 5-10 μm wide) structured crystal which behaves as a light guide pipe for scintillation light. The pipes prevent the scattering of the optical photons in the crystal medium and collimate them onto the photosensor array. Theoretically, a thicker layer of structured scintillators can be used to increase the absorption efficiency of the detector without degrading spatial resolution. Disadvantages of this design include the fragility and the hygroscopicity of the CsI crystals. In addition, due to internal crystal defects of the CsI, guiding capabilities are still poor [44]. In addition, the multi-step conversion process leads to reduced conversion efficiency - a significant disadvantage attributed in all indirect conversion detectors.

2.1.2 Direct conversion detection

Direct conversion detectors use a photoconductive material instead of a scintillator-photosensor combination making the conversion process a single step. In the majority of direct conversion detectors the photoconductor is sandwiched between two electrodes,

and a high electric field is applied between them. The absorbed x-rays are converted into electron-hole pairs (EHP) primarily via either the photoelectric effect or Compton scattering. Under the action of an applied electric field, electrons and holes drift towards their respective oppositely charged electrodes where an external electronic system collects them. The high electric field is required to avoid the recombination of charge carriers and suppresses their lateral diffusion thus providing high spatial resolution. The number of generated and collected EHP per absorbed photon governs the sensitivity of the detector. A schematic presentation of the direct conversion approach is shown in Fig. 2.3.

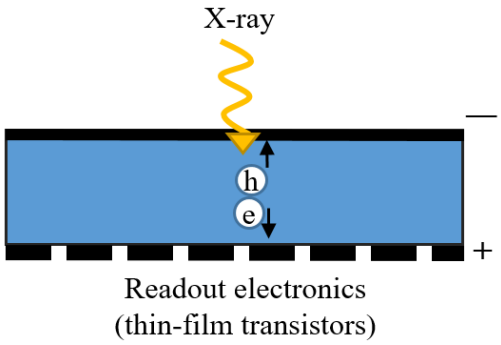

Figure 2.3. A schematic presentation of the direct conversion detector operation.

Direct conversion detectors possess several advantages over indirect ones. The elimination of scintillators and photosensors with optical coupling increases the charge collection efficiency of the detector by reducing the charge loss which ultimately occurs at each conversion step. Electrons and holes drift towards the electrodes along the lines of applied electric field meaning the lateral spread of charge carriers is minimal. The spatial resolution is limited only by the fundamental x-ray interaction physics and the size of the pixels on the collecting electrode which can be made higher than indirect conversion. Therefore, a relatively thick semiconductor material can be used to achieve optimal absorption efficiency without a decrease in the image quality due to image blur (Fig. 2.4).

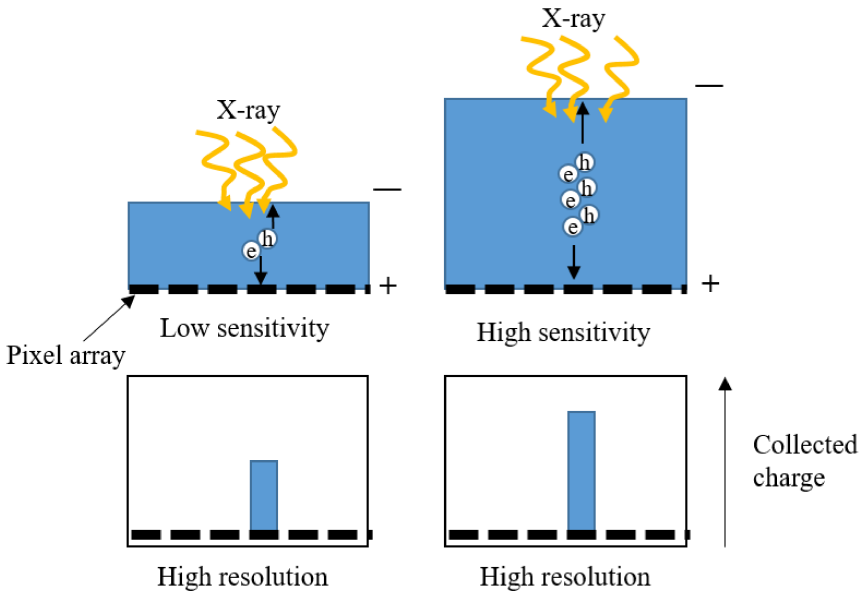

Figure 2.4. A schematic diagram of direct conversion process for thick and thin semiconductors. Thicker material increases the absorption without degradation in spatial resolution [44].

2.2 Attenuation of X-rays in a medium

For over a decade, direct conversion detectors have been demonstrating excellent performance, providing high-resolution and high-sensitivity digital imaging [45]. The properties of the radiation detection medium primarily determine the imaging performance of the detector. There are several possible outcomes after ionizing radiation impinges on a detector: 1) the photon may transfer all its energy to the medium after absorption; 2) the photon can be scattered in a different direction; 3) or the photon can pass through the detector without interaction. Photons that pass through the material are usually called primary photons or primary radiation, while photons that experience scattering or absorption and have been attenuated are regarded as secondary radiation. The process of x-ray beam attenuation refers to the removal of photons from the beam while it propagates through the medium. The attenuation of the x-ray beam can be obtained by considering the number of absorbed and scattered photons of the beam *dI* in a thin slice *ds* of the medium in proportion to the intensity *I(s)* of the beam in the same slice:

$$\frac{dI}{ds} = -\mu I(s) \tag{2.1}$$

The result of solving the differential equation is:

$$I(s) = I_0 e^{-\mu s} \tag{2.2}$$

where I_0 is the incident x-ray flux intensity, s is the material thickness and μ is referred as linear attenuation coefficient of the absorber in units of [cm^{-1}]. The value of μ depends on the physical density, the atomic number of the material, and the energy of incident x-ray.

The use of a linear attenuation coefficient can be problematic in cases where the density of the material changes. Another way of expressing the attenuation of the beam that is independent of density is a mass attenuation coefficient μ_m. The mass attenuation coefficient can be derived by dividing the linear attenuation coefficient by the density of the material and is expressed in [cm^2/g]:

$$\mu_m = \frac{\mu}{\rho} \tag{2.3}$$

where ρ is the density of the absorber. The attenuation coefficient may be expressed in other units like the atomic attenuation coefficient μ_a [cm^2/atom] given by:

$$\mu_a = \frac{\mu M}{\rho N_a} \tag{2.4}$$

Or the electronic attenuation μ_e [cm^2/electron] coefficient:

$$\mu_e = \frac{\mu_a}{Z} = \frac{\mu M}{\rho N_a Z} \tag{2.5}$$

where M is the molecular weight, N_a is Avogadro's number and Z is an effective atomic number.

2.3 Mechanisms of x-ray and γ-ray interaction with matter

An x-ray (γ-ray) in a diagnostic energy range can interact with matter in several deferent ways: photoelectric absorption, coherent scattering (Rayleigh scattering), Compton scattering and pair production. The probability of the photon propagating in a medium of thickness x without interaction ($e^{-\mu x}$) is given by:

$$e^{-\mu x} = e^{-\omega x} e^{-\tau x} e^{-\sigma x} e^{-\kappa x} = e^{-(\omega+\tau+\sigma+\kappa)x} \tag{2.6}$$

where the probabilities that the photon does not interact by specific mechanisms are shown by: $e^{-\omega x}$ in case of coherent scattering, $e^{-\tau x}$ is photoelectric absorption, $e^{-\sigma x}$ is

Compton scattering and $e^{-\kappa x}$ is the pair production mechanism. Each coefficient can be expressed as mass, atom or electronic coefficients similar to the linear attenuation coefficient mentioned before.

2.3.1 Photoelectric effect

In the photoelectric effect, all the energy of the incident photon is transferred to an orbital (usually K-shell) electron (Fig. 2.5) which is ejected from the atom and henceforth termed as the primary photoelectron.

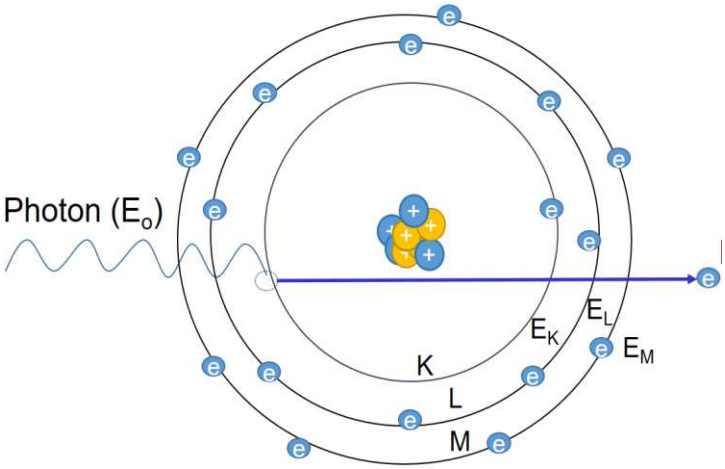

Figure 2.5. Photoelectric absorption with primary electron ejected from the k-shell orbital.

The kinetic energy of the photoelectron (E_p) is equal to the incident photon energy (E_0) minus the binding energy of the ejected photoelectron (E_K):

$$E_p = E_0 - E_K \tag{2.7}$$

The photoelectric effect will not occur if the energy of the incident photon is less than the binding energy of the orbital electron. The photoelectron leaves the atom with a vacancy which will be filled by cascading electrons from other energy levels resulting in emission of characteristic photons and Auger electrons. The energies of the characteristic photons are usually less than 0.5 keV meaning that they will be absorbed easily in the material in close proximity to the interaction point. Having large kinetic energy, the ejected photoelectron will excite atoms when interacting with the crystal lattice and will create many secondary EHP's along its passage. Those EHP will be collected via the

external circuitry. The probability of the photoelectric effect (τ_p) increases with the atomic number Z of the material and can expressed as [45]:

$$\tau_p = \frac{Z^3}{E^3} \tag{2.8}$$

where E is the energy of the incident photon.

The advantage of the photoelectric effect for imaging applications is a lack of scattered photons. Scattered photons would be absorbed over a distance from the point of interaction and therefore cause image blur and degrade the image quality. From Eq. (2.8) it is seen that the photoelectric effect dominates when lower energy photons interact with high Z material, and that is why semiconductors with high Z are an appealing option as x-ray (gamma-ray)-to-charge transducers in the diagnostic energy range. The relationship between the probability of the photoelectric effect, as a function of the atomic number, and photon energy is shown in Fig. 2.6.

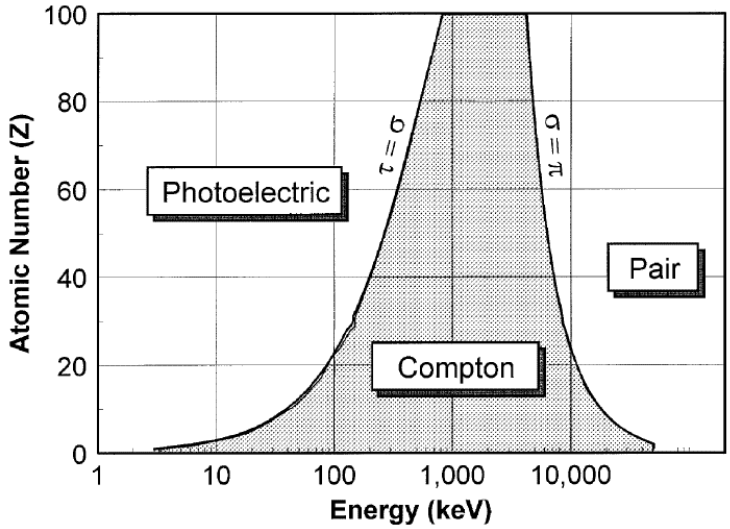

Figure 2.6. The region where each x-ray interaction process is more likely to occur as a function of atomic number and x-ray energy [46].

2.3.2 Coherent (Rayleigh) scattering

The mechanism of Rayleigh Scattering can be described as an interaction between the incident photon and an atom as a whole. Subsequently, the atom's electron cloud starts to oscillate. The result of this oscillation is the remission of a photon with the same energy as the incident photon. However, the emitted photon experiences a change in its trajectory relative to the incident x-ray photon. In contrast to the photoelectric effect, no

electron is ejected from the atom, and thus ionization of the atom does not occur. The change in photon trajectory (or scattering) has a detrimental effect on image quality since subsequent reabsorption of the scattered photon causes an image blur. The scattering angle increases at small x-ray energies as shown in Fig. 2.7. Rayleigh scattering is the most probable interaction for low energy x-rays with high *Z* materials.

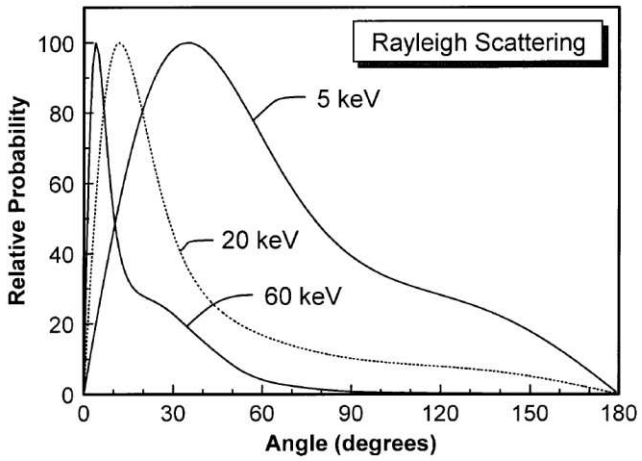

Figure 2.7. Probability density functions for Rayleigh scattering angles for different energies in water [46].

2.3.3 Compton scattering

Compton scattering is the most likely interaction between an incident x-ray or γ-ray photon with an outer shell (free) electron in the diagnostic energy range. This interaction is also inelastic, incoherent, and non-classical scattering. An incoming high energy photon transfers some of its energy to an outer shell electron and ejects it from the atom as shown in Fig. 2.8. Due to the comparatively low binding energy of outer shell electrons, they are usually ignored in further energy calculations. The Compton interaction results in the ionization of the atom and the splitting of the incident photon's energy between the ejected electron and the scattered photon.

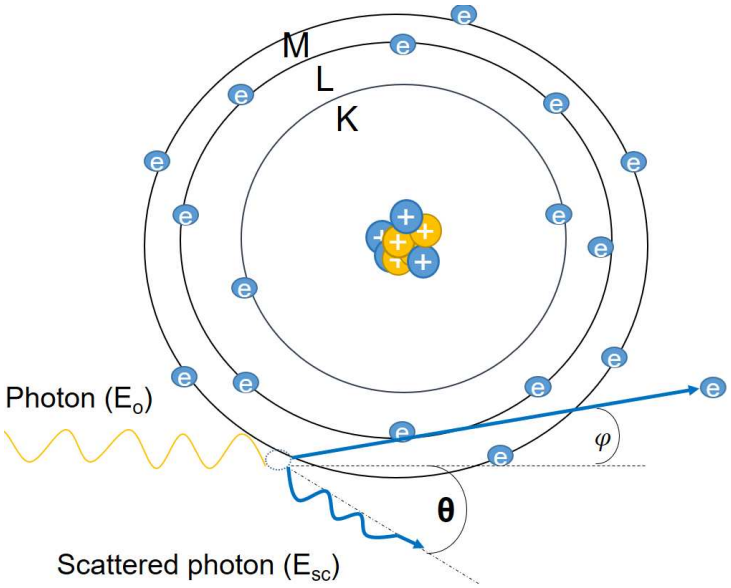

Figure 2.8. Schematic diagram of Compton scattering interaction

The binding energy of the ejected electron can be calculated as:

$$E_e = E_0 - E_{sc} \tag{2.9}$$

where E_{sc} is the energy of scattered photon, E_0 is the energy of incident photon. The energy of the scattered photon can be calculated using the Klein-Nishina [46] formula:

$$\frac{E_{sc}}{E_0} = \frac{1}{1+\alpha(1-\cos\theta)} \tag{2.10}$$

where

$$\alpha = \frac{E_0}{m_0 c^2} = \frac{E_0}{511keV} \tag{2.11}$$

and where θ is the angle of the scattered photon and $m_0 c^2$ is the rest mas of the electron. The conservation of energy and momentum requires the energy of the scattered photon to decrease with increase of the angle of the scattered photon θ as predicted by the Compton process (eq. 2.10-2.11). The ejected electron interacts with surrounding atoms in the crystal lattice and loses its kinetic energy generating secondary EHP's along its path. The relationship between the probability of Compton scattering, the atomic number and photon energy is shown in Fig. 2.6.

2.3.4 Pair production

Pair production can only occur when the photon energy exceeds 1.02 MeV. Pair production results from the interaction of an incident high energy photon with the electric field of the nucleus of an atom. The interaction leads to the complete absorption of the photon and creation of an electron-positron pair. Since energy must be conserved, for an incident photon with energy E_0:

$$E_0 = E_+ + m_0c^2 + E_- + m_0c^2 \tag{2.12}$$

where E_+ and E_- are the kinetic energies of positron and electron respectively. The energy threshold 1.02 MeV can be explained by the rest mass of electron m_0c^2 which is equivalent to 511 keV. After creation, the positron travels some distance in the medium until it interacts with a negatively charged electron. As a result, electron-positron annihilation process takes place. The annihilation process requires conservation of energy and momentum thus the two photons are emitted in almost opposite directions with energies of 511 keV. A schematic presentation of the pair production interaction is shown in Fig. 2.9.

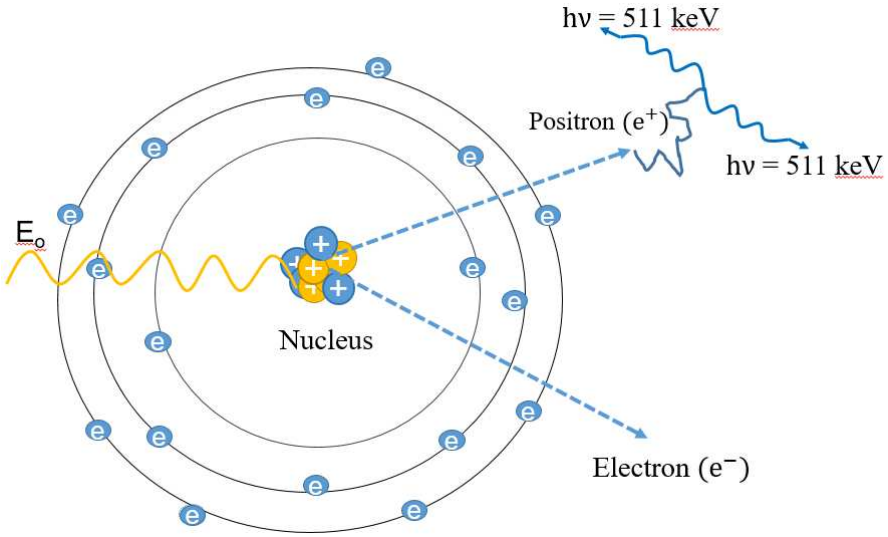

Figure 2.9. Pair production caused by the collision of a photon with energy $E_0 \geq 1.022$ MeV with an atomic nucleus.

Pair production is not a typical mechanism of interaction in diagnostic imaging as the threshold energy required for pair production is far beyond the energy range used.

2.3.5 CdZnTe as a direct conversion detector

The five most important criteria when potential photoconductors are considered for radiation medical imaging detectors applications are: (1) high absorption efficiency via photoelectric absorption; (2) high x-ray (or gamma ray) – to-charge conversion gain; (3) good photoconductive properties; (4) low dark current and (5) compatibility with large area detector technology. CdZnTe satisfies all criteria. First of all, it has a high density (5.78 g/cm^3) due to the high atomic numbers of Cd (Z=48), Te (Z=52) and Zn (Z=30) [45]; and a wide band gap (1.52 – 1.57 eV [5, 9]). The primary mechanism (~95%) of photon interaction in CdZnTe within the diagnostic energy range is photoelectric absorption. Fig. 2.10 shows the photoelectric component of different semiconductors as a function of photon energy.

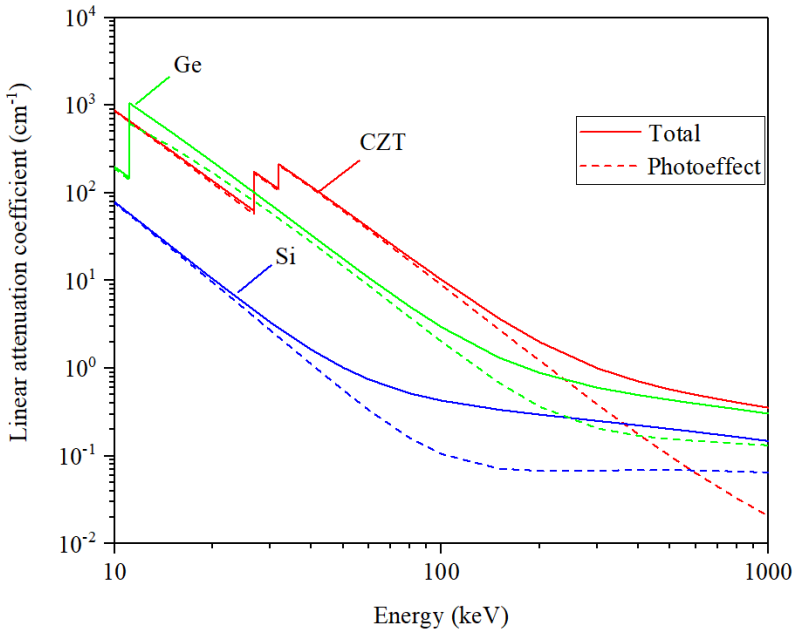

Figure 2.10. Linear attenuation coefficients as a function of photon energy for different photoconductors [47].

Both types of photogenerated carriers are mobile in CdZnTe and possess high drift mobility (especially electrons). At the same time, dark resistivity is high due to the wide bandgap and recent advances in fabrication technologies produce CdZnTe samples with low defect concentrations which also provides a low dark current, which is very important for a high signal-to-noise ratio and good image contrast. As for the x-ray-to-charge conversion gain, as with many crystalline semiconductors, in accord with the

Klein rule [48, 49] the energy required to generate an EHP or the ionization energy ($W_{\pm}$) is proportional to the band gap as $W_{\pm} \approx 3E_g$. A narrower bandgap means that more EHP's will be generated from the absorbed photon leading to an increase in the resulting signal, however there is a trade-off between high resistivity and the small ionization energy to keep a high signal-to-noise ratio. The bandgap of CdZnTe is 1.52 – 1.57 eV which should result in an EHP creation energy of $W_{\pm}$ = 4.56-4.71 eV/ehp which is comparatively low [49].

Another advantage of CdZnTe is the ability to operate at room temperature in contrast to germanium which requires additional cooling by liquid nitrogen due to the high internal dark currents (result of the small band gap). Consequently, the use of germanium detectors is unfeasible for numerous medical imaging applications.

2.4 CdZnTe applications and their requirements

Other important factors which define the applicability of a material for imaging applications are energy and spatial resolution. Energy resolution determines the efficiency of the detector to differentiate between photons of different energies and to discriminate Compton scattering.

Energy resolution can be determined by recording the response of the detector to a monoenergetic radioactive source. The illustration of the theoretical pulse height spectrum and actual spectra produced by a detector when it is exposed to a source emitting $E_{0,}$ is shown in Fig. 2.11. As mentioned in section 2.3, the main interaction of x-rays and γ-rays with the photodetector in the diagnostic energy range is photoelectric absorption and Compton scattering. The photoelectric interaction leads to the complete deposition of the photon energy and corresponds to the straight vertical red line in Fig. 2.11. The peak position of the ideal spectrum corresponds to the energy of the fully absorbed photon (E_0). The Compton-scattering interactions result in partial energy transfer to the detector leading to energies lower than E_0. The influence of Compton scattered photons from different parts of the detector (or its components) causes blurring and reduces the contrast in the image.

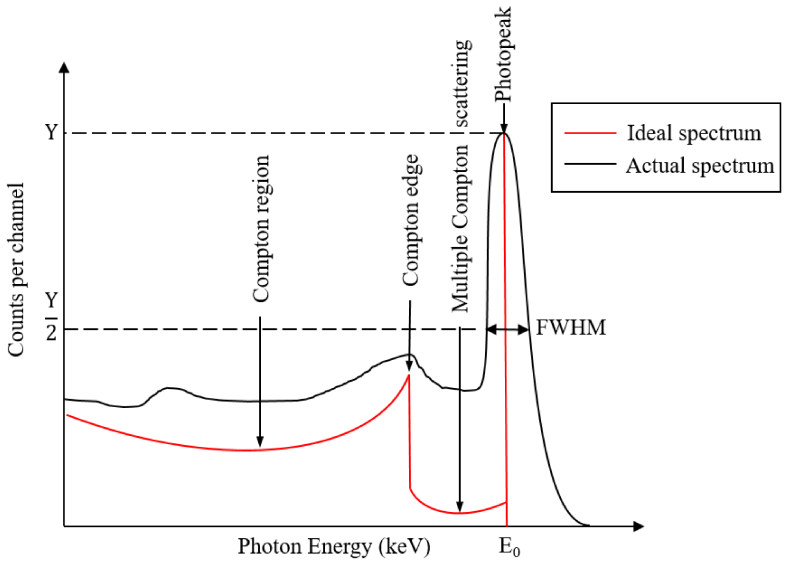

Figure 2.11. Distribution of energies deposited in a theoretical detector. The red line corresponds to an ideal spectrum while the black line shows the actual spectrum of energies. Note: Compton edge corresponds to the energy of the ejected electron in a 180-degree scattered event.

From Fig. 2.11 it can be seen that sharp edges and clear lines in the ideal spectrum become broadened and rounded in the actual detector. The broadening can be explained by the statistical effects (e.g., statistical noise) that occur during the charge generation and detection processes. The width of the peak distribution at half the maximum height of the peak is called the full width of half maximum (FWHM). The energy resolution of the detector is normally defined as the FWHM divided by the pulse amplitude at the centre of the peak:

$$R = \frac{FWHM}{E_0} 100\% \tag{2.13}$$

The energy resolution R is a dimensionless value that is typically converted to a percentage.

To sum up, it should be stated that the narrower the photopeak, the more efficiently a detector will differentiate between photons created via Compton-scattering and the photoelectric effect. For medical imaging applications, this will benefit image quality since contrast will be improved.

Spatial resolution is the ability of the imaging device to provide the certain level of detail and sharpness in the image. One of the major factors that limit the sharpness of the

images is the intrinsic resolution of the imaging detector. The intrinsic spatial resolution can be estimated by placing a specially designed phantom directly on the detection system and irradiating it with a point source located opposite the phantom at several meters distance. Spatial resolution is expressed as the smallest object visible on the image.

The influence of energy and spatial resolution on a CdZnTe detector's performance in a variety of applications is discussed in the following subsection.

2.4.1 Medical imaging

Research interest in the development of a detector for medical imaging based on CdZnTe increased in the late 90s [8, 45] when this material was first considered for direct conversion gamma cameras. Before 1998, most gamma cameras used an indirect conversion scheme with large scintillation crystals (mainly Na(I)) outfitted with an absorptive parallel-hole collimator optically coupled to a 2D array of vacuum photomultiplier tubes (PMT) connected in turn to external electronics and output devices. This design was first introduced by Hal Anger in 1958 [50]. The basic principle and design of an Anger gamma camera is shown in Fig. 2.12.

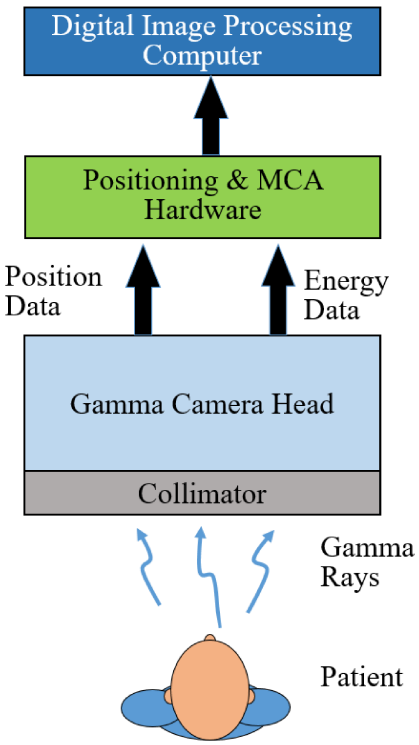

Figure 2.12. Basic principles and components of the Anger gamma camera.

After emission from patient's body, high energy photons impinge on the surface of the scintillation crystal through a collimator. The scintillation light is detected by PMTs which are optically coupled to the back of the scintillation crystal. Information on the energy deposited by the photon interaction with the scintillator is obtained by summing the signal outputs of all PMTs while decoding the hit position and involves deriving the distribution of signals across the array of PMTs (i.e., weighting the outputs of several adjacent PMTs in the array). Often manufacturers utilize plastic light guides between the PMT array and the scintillation crystal to increase the light collection efficiency by collimating the light straight to the PM tubes and avoid gaps between them. In photon-counting gamma cameras, each pulse from the individual photon is read by tightly fitting readout electronics and a sense amplifier that shapes the analog signal with an amplitude proportional to the incident x-ray photon energy. The amplifier is connected to N independent discriminators and counters with digitally adjustable threshold values. Each counter counts the number of pulses with an amplitude above the established threshold level. Ultimately, data collection yields N sets of photons counts with different energy thresholds called energy bins. The final x-ray image is divided into N quasi-monochromatic images generated in one acquisition with an optimal contrast-to-noise ratio. Using relevant software and a high-end computer, various multispectral imaging methods (like dual-energy subtraction imaging and material decomposition techniques) can be performed with the acquired data.

The intrinsic spatial resolution of gamma cameras based on a NaI scintillators is about 3-4 mm [6]. The actual spatial resolution of the system is much worse than the intrinsic one, especially when high-sensitivity low-resolution collimators are used. Practically, system spatial resolution in modern NaI gamma cameras does not exceed 6-8 mm.

Energy resolution is another important characteristic of a single-photon imaging gamma camera since it influences the ability to remove photons that have lost energy via Compton scattering from the image data and reduce image blur. In the state-of-the-art clinical NaI gamma cameras, energy resolution can reach ~11% at 140keV and ~16% at 60keV [6].

Despite the fact that scintillation Anger gamma cameras are highly effective instruments, they do have a number of undesirable aspects including the use of fragile and costly PMT tubes, an inability to work in a magnetic field, and the possibility of damaging a scintillator with an abrupt temperature change. The disadvantages mentioned above and the clinical need for detectors with millimeter (or even sub-millimeter) spatial resolution and higher energy resolution motivated the scientific community to consider replacing the Anger design with a direct conversion detection scheme using a semiconductor material. First attempts to improve the technology, concentrated on Germanium detectors, which failed because of the required liquid nitrogen cooling and inefficient stopping power.

One of the best candidates for a material for gamma-camera applications is CdZnTe due to its higher intrinsic energy resolution compared with NaI scintillators [6]. The first problem that scientists faced was the limited availability of large volume CdZnTe samples. Since the growth processes did not allow for the preparation of a large area crystals, IMARAD Imaging Systems [51, 52] found a solution by taking separate tileable CdZnTe detector modules and connecting them in a 2D matrix to achieve the desired field of view (FOV). IMARAD used a Bridgman method to grow 5 mm thick CdZnTe modules 40mm x 40mm in size. One face of the detector was covered by an array of 16 x 16 pixelated metal electrodes with a pitch of 2.5 mm, while the opposite face had a continuous contact. Segmentation of the radiation detectors with an individual pixel electrode read-out allows improvements in the intrinsic spatial resolution in contrast to the signal weighting scheme regardless of the initial photon energy. Pixelated IMARAD detectors demonstrated a high resistivity, around $5x10^9$ Ωcm^{-3}, and high energy resolution (about 5% at energy 140 keV).

The modular CdZnTe detector technology was successfully used by DIGIRAD in 1997 [53] who marketed the first commercially available mobile gamma camera named the "Digirad 2020tc Imager™". The imaging system consisted of 64 tightly packed detector modules with additional readout electronics for signal processing and detachable conventional collimators for nuclear imaging. Each detector module was 25mm x 25mm x 12mm in size making the total active imaging area of 20cm x 20cm. The Digirad 2020tc Imager™ was developed to study organ anatomy and to perform a

wide range of operations such as scintimammography, bone scans or cardiac imaging. A superb energy resolution of ~5% was obtained by using a Co-57 source and compares with ~10% achieved by Anger type gamma cameras based on the NaI(TI) scintillator detector at 140keV.

A few years later in 2002, the Israeli national laboratory Soreq Nuclear Research Center (Soreq NRC) developed a gamma camera based on CdZnTe and named it the NUCAM 3 that was designed for breast scintimammography and cardiac SPECT [54]. The imaging system demonstrated by Soreq contained 528 segmented closely packed monolithic CdZnTe detectors with readout electronics. Each pixelated detector was 5 mm thick with a pixel pitch of 2.1 mm making the overall FOV 18.6 cm x 20.1 cm. The system also included a square parallel-hole (1.9 mm x 1.9 mm) lead collimator needed for the creation of the two-dimensional projection images of the radiotracer distribution. The energy resolution achieved by the Soreq NRC with the NUCAM 3 system was 4.5% at 140.5 keV and ~9.5% at 59.6 keV and spatial resolution was about 2.1mm was achieved, regardless of the incident photon energy.

The successes with gamma camera systems based on CdZnTe increased the research effort to use solid-state CdZnTe detectors for Molecular Breast Imaging (MBI) applications. MBI is an imaging modality that utilizes gamma cameras in a mammographic configuration to provide functional breast images with high resolution and sensitivity. The Anger detection scheme is suboptimal for MBI for several reasons. First of all, the actual FOV of Anger gamma cameras are significantly smaller than the detector size because of the presence of the dead space at the edges of the camera. This dead space is caused by the difficulty in resolving hit events beyond the center of the last PMT tube and prohibits mammography-like design with two detectors placed on both sides of a slightly compressed breast. Consequently, a patient should be imaged with the camera positioned laterally which results in an increased distance between the detector and the breast and leads to a decrease in spatial resolution and decreases the ability to detect small breast lesions. In addition, in a lateral position, the gamma camera will acquire the vast majority of counts coming from the heart and liver thus degrading the sensitivity to the breast.

One of the outstanding features of a CdZnTe-based detection system is the ability to customize the camera design specifically for breast imaging and to (1) offer better spatial resolution to improve the detection of small lesions and (2) to improve energy resolution and obtain better image contrast through more efficient rejection of scattered events. Blevis et al. [55] and Muller et al. [56] proved that the seamless connection of individual CdZnTe detector modules in a 2D array provides a FOV that is almost identical to gamma camera dimensions with no image artifacts and minimal dead space at the edges. They published very promising results for a compact CdZnTe gamma camera for scintimammography - a predecessor of the MBI devices. Both research groups concluded that the image quality of close objects obtained by the CdZnTe gamma camera was superior to that of Anger gamma cameras using NaI scintillators. Results showed a considerable improvement in tumour detectability, especially for tumours of 5 mm in size.

Based on the success of the CdZnTe scintimammography camera, GE Healthcare, recently employed CdZnTe in a device for myocardial perfusion imaging called the Discovery NM 530 (DNM) [57]. The cardiac SPECT camera consists of a 16x16 array of detector modules with 4x4x0.5 cm^3 pixelated CdZnTe crystals. The multi-pinhole collimator block provides direct illumination of the CdZnTe gamma detector. Published data demonstrates a system energy resolution of 5.4% at 140 keV for Tc-99m and a spatial resolution of ~5mm which is significantly higher than conventional dual-headed standard SPECT cameras [57].

To summarize, the best solid-state material for gamma cameras currently is CdZnTe due to the excellent energy resolution and superb intrinsic spatial resolution which is limited only by the size of the pixel electrode. This makes CdZnTe an attractive material for use in computed tomography (CT) since the energy range used in CT is similar to energies used in the applications described above. However, CT operates at much larger photon fluxes than those used in nuclear medicine. As a result, the charge generation rates in CT are much larger. This, in turn, requires an x-ray-to-charge transducer with excellent transport properties to prevent possible accumulation of the generated charge, to avoid a polarization effect, the distortion of the internal electric field, and as a result degradation in image quality. This calls for a material with high mobility

for both types of carriers. Given that CdZnTe has comparatively low hole mobility, charge transport in this material should be carefully examined for compatibility with CT imaging requirements and/or to provide suggestions for how it can be improved to fit CT requirements.

Chapter 3: Computed tomography (CT)

The most significant clinical advantage of the computed tomography is the ability to reconstruct a detailed 3D image of human body anatomy.

3.1 Basic principles of operation

The basic principle of computed tomography is to obtain a large number cross-sectional x-ray images ("slices") at multiple angles and mathematically reconstruct the 3D image from the acquired data as shown in Fig.3.1.

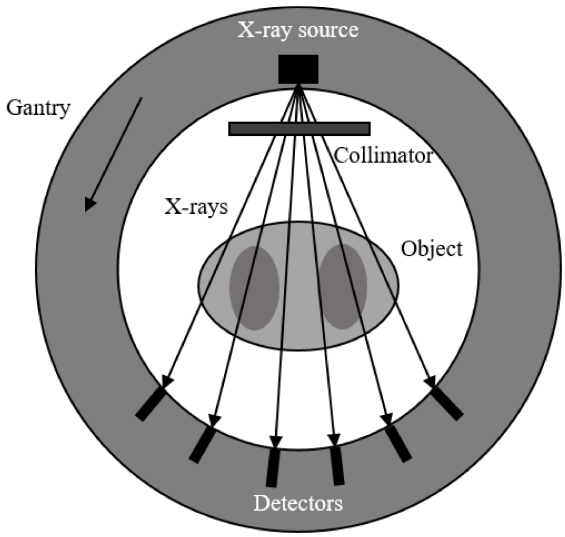

Figure 3.1. Schematic illustration of 3D CT scanner.

In CT, the stationary object is surrounded by a rotating circle termed a gantry. The x-ray tube and collimator are mounted on this gantry opposite to an arc-shaped row of detectors, thus each detector has a fixed position relative to the x-ray source. Current CT manufacturers utilize a conventional detector design based on an indirect conversion scheme operated in current mode (detector measures average rates of photon flux) without energy discrimination. Such designs consist of three major layers: scintillation crystal, photodiodes and analog readout electronics. The detectors are packed into modules (detector arrays) for better detection accuracy. The x-rays emitted by the tube

are attenuated by the patient's body and registered by the detection system opposite to the patient. The transmission of an x-ray through the patient can be expressed as:

$$I(s) = I_0 e^{-\sum \mu_i s_i} \tag{3.1}$$

It is impossible to calculate the particular linear attenuation coefficients for each body part from the single transmission thus the gantry performs a 360-degree rotation, and the detectors collect attenuated beams through the body from different orientations that allow calculation of separate attenuation coefficients μ_i. As a result, each slice of the body can be expressed as a matrix of the attenuation values of the cross-section. Each attenuation value is converted to a CT numbers using the expression:

$$CT\_number = 1000[\frac{\mu_i - \mu_w}{\mu_w}] \tag{3.2}$$

where μ_i is a mean attenuation of the element of tissue (called a voxel) that extends through the thickness of the cross-section, and μ_w is the linear attenuation coefficient of distilled water.

From the Eq. 3.2 it can be seen that the CT number will have a positive value if the attenuation coefficient of the irradiated material is higher than water (bones, muscles) whereas a negative CT number will correspond to materials with lower attenuation coefficient (lungs). After assigning each CT number a particular shade of gray, the matrixes of attenuation values can be shown as gray-scale displays which are combined mathematically in the final 3D CT image representation.

3.3 Advanced CT and detector requirements

Applications in advanced computed tomography, which are usually called spectral CT or photon-counting computed tomography (PCCT), requires detector performance which is challenging to achieve with conventional detector technology. In photon-counting imaging, it is vital to count each incident x-ray photon and at the same time precisely measure the energy. To satisfy these requirements, a detector with the ability to discriminate photon energy is needed, which in turn requires high energy resolution. As was evident from the review, the energy resolution of CdZnTe detectors is much higher than indirect conversion detectors. This combined with the high spatial resolution, high stopping power with the photoelectric effect being the primary

interaction in the CT diagnostic range (30-140 keV), and the ability to operate at room temperature, makes CdZnTe the most promising semiconductor material for photon counting CT.

Although very promising due to high energy resolution, CdZnTe detectors have never been tested with high x-ray flux. The high flux rate required in CT (> 10^9 photon/(mm^2s)) puts a stringent requirement on detector properties and, most importantly, on electron and hole drift mobility. Indeed, unless the detector material has adequate transport properties, under high x-ray flux the charge-generation rate can become higher than the charge removal rate and excess charge will build up causing a dynamic polarization effect that is proportional to the photon flux. The situation becomes more complicated in the presence of compensating dopants [42] and structural defects which act as carrier traps so that a significant portion of the x-ray generated charge carriers can be trapped forming space charge and disturbing the internal electric field further.

The high potential of CdZnTe in CT has resulted in a large number of studies to improve CdZnTe crystallinity as well as to investigate the transport properties of the resulting material. In collaboration with Philips Healthcare, we are carrying out a project on CdZnTe detectors for advanced CT. As will be explained below, CdZnTe properties are investigated using several experimental techniques including optical time-of-flight, charge extraction by linearly increasing voltage (CELIV), and pulse height spectroscopy techniques. The major experimental method used is TOF due to its proven efficacy in determining the transport properties of CdZnTe. However, we extend the conventional TOF theory to account for the influence of a space charge distribution on the transport properties and the key electrodynamic parameters such as the electric potential and the internal electric field distribution.

3. Measurements of transport properties in CdZnTe semiconductor for application in CT

4.1 Materials and methods

Two 2 mm-thick CdZnTe block detectors were manufactured by Redlen Technologies. The samples were provided with a pixelated array of electrodes (0.5 mm

x 0.5 mm each) on one detector face and with a continuous semitransparent metal electrode on the opposite face. In order to increase the signal magnitude for electro-optical measurements and to avoid the small pixel effect, several pixels were connected together. For sample #1 this was achieved by applying a conductive polymer (AGFA Orgacon-Pedot) atop the pixelated array to provide a ~50 mm^2 electrode, semitransparent to the blue light (Fig. 4.1). In contrast, for sample # 2, a 100 Å gold coating was deposited to provide ~55mm^2 electrode (Fig. 4.2). For both samples, additional Indium bump bonding was applied on the top of the gold/Pedot contacts to protect them from possible scratches and damage by the connector pin. Prior to performing the electro-optical characterization, the dark current I_d and the resistivity of the samples were measured at the selected bias voltages of +200 V and -200 V applied to a continuous metal electrode. The obtained data are shown in Table 4.1.

Table 4.1 Characteristics of the CdZnTe samples

Sample #	Thickness [cm]	Contact area [cm^2]	ρ (+200V) [Ωcm]	ρ (-200V) [Ωcm]	I_d (+200V) [nA]	I_d (-200V) [nA]
1	0.2	0.5	10^9	10^{10}	485	47
2	0.2	0.55	10^{10}	$2.2x10^{11}$	55	2.5

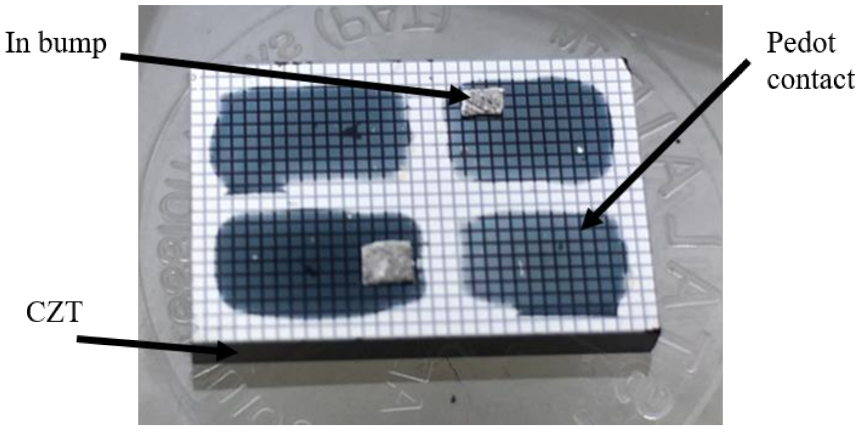

Figure 4.1. The CdZnTe sample #1 with a pixelated top electrode. AGFA Orgacon-Pedot was used to connect several pixels.

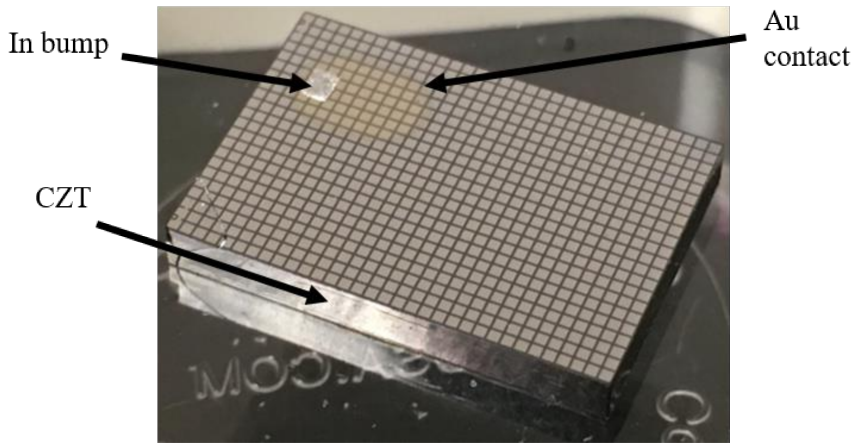

Figure 4.2. The CdZnTe sample #2 with a pixelated top electrode. A thin layer of gold was used to connect several pixels.

4.2 Optical time of flight technique (TOF)

The basic principles of the TOF technique was provided in Section 1.4. Below we present the details of the TOF apparatus used as well as major results on electron and hole transport in our CdZnTe samples.

4.2.1 Experimental apparatus

The typical TOF experimental apparatus is shown in Fig. 4.3. For the TOF measurements the electric field across the CdZnTe layer was created by applying a negative bias to the continuous electrode, since this polarity provided the lower dark current values (see Table 4.1). For measuring hole drift mobilities, the sample was illuminated through the pixellated electrode face, as shown in Fig.4.3, while for measuring electron mobilities the light was incident on the continuous electrode face. The attenuator controlled the light intensity, impinging on the CdZnTe. The low level of light intensity was determined by the CdZnTe sensitivity (i.e. the lowest intensity, which provided clear signal), while the upper level corresponds to 15 times the low level intensity.

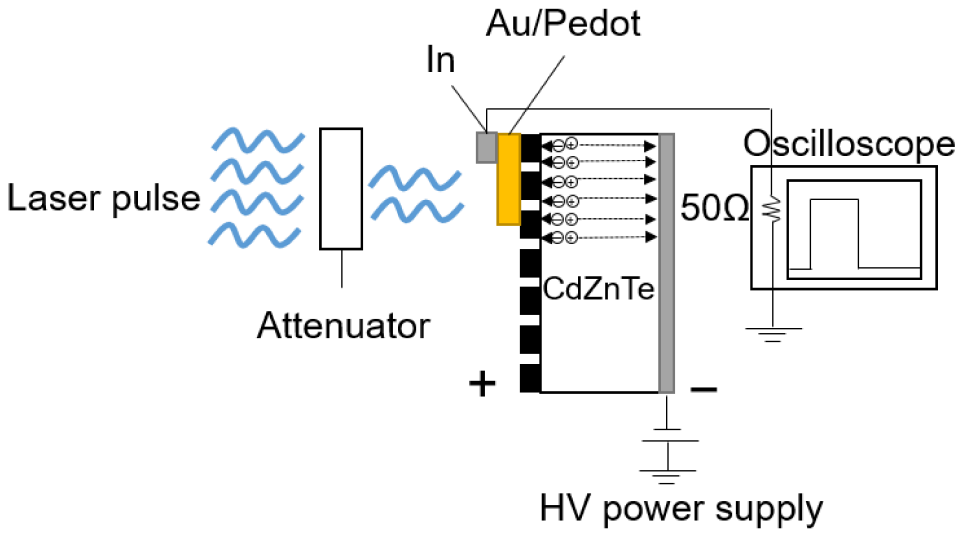

Figure 4.3. Schematic diagram of the TOF setup.

TOF measurements were performed in a wide range of electric fields with an upper value of 4000 Vcm^{-1} defined by typical CdZnTe operating voltage. To comply with TOF requirements, highly absorbed light ($\lambda = 430$ nm) was used to generate electron-hole pairs close to the contact/CdZnTe interface [31]. Thus, one type of photogenerated carriers was immediately collected by the adjacent electrode, while another type of carriers was drawn across the layer under the influence of the applied field. The laser pulse duration was 35 ps, which is much smaller than the expected charge carrier transit time (~ns for electrons and ~μs for holes), as required for accurate TOF measurements. To measure the temperature dependencies of the carrier mobilities the sample was placed on a LINKAM LTS350 cooling-heating stage which allows for precise temperature control over a wide temperature range from 193 K to 433 K. For the room temperature measurements, the TOF signals were recorded on 6 GHz bandwidth oscilloscope with a built-in 50 Ω termination resistor (without any amplifiers). For other temperatures, a Tektronix TDS 2024C oscilloscope was used with a 50 Ω resistance connected in parallel with the scope.

4.2.2 Results

a. Sample #1

i. TOF of electrons

The typical TOF signal for electrons, measured on sample #1 is shown in Fig. 4.4. The TOF transient has a quasi-rectangular shape with a well-defined knee, representing the electron transit time $t_{transit}$. Insert to Fig. 4.4 shows the TOF transient for electrons at ~15 times larger light intensity. The TOF signal is no longer the quasi-rectangular, but rather represented by a cusp, followed by the gradual roll-off of the photocurrent. The deformation of the shape of the TOF transient at higher light intensity shows the polarization effect, manifested by the distortion of the electric field inside the material. In this case, the transit time of the fastest carriers is derived from the cusp position and normally equals 0.8 times the $t_{transit}$ value, measured at low intensity, as predicted by the polarization effect model [58].

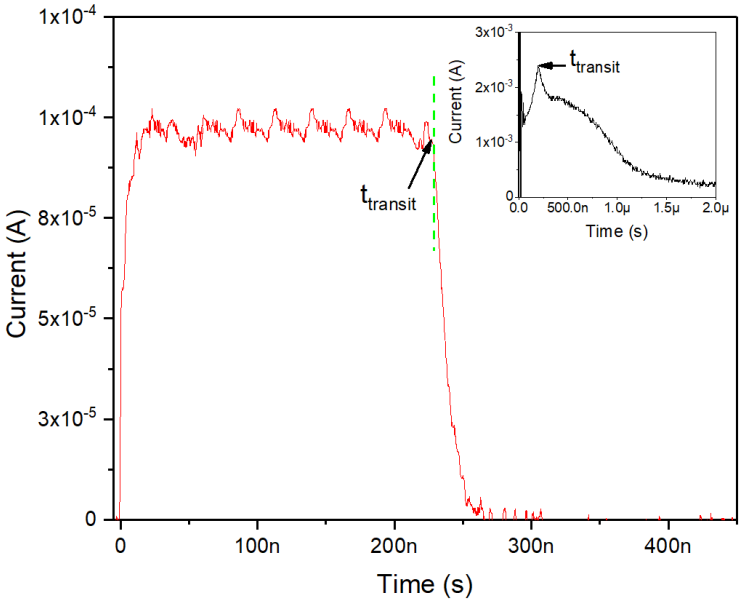

Figure 4.4. The TOF signal for electrons measured at -200V applied to the continuous electrode. The measurements were performed at low and high light intensities represented by the red and black (inset to the figure) curves, respectively.

The electron drift velocity was calculated from the $t_{transit}$, measured at low light intensity, using Eq. 1.2. Fig. 4.5 show the obtained drift velocities plotted as a function of the electric field for different temperatures from 293 K (RT) to 433 K. As seen from Fig. 4.5, the electron drift velocities depend linearly on the electric field at all temperatures, indicating a field-independent electron mobility, which was derived from the slope of the drift velocity according to Eq. 1.3. Both electron drift velocity and mobility were found to decrease with increasing temperature.

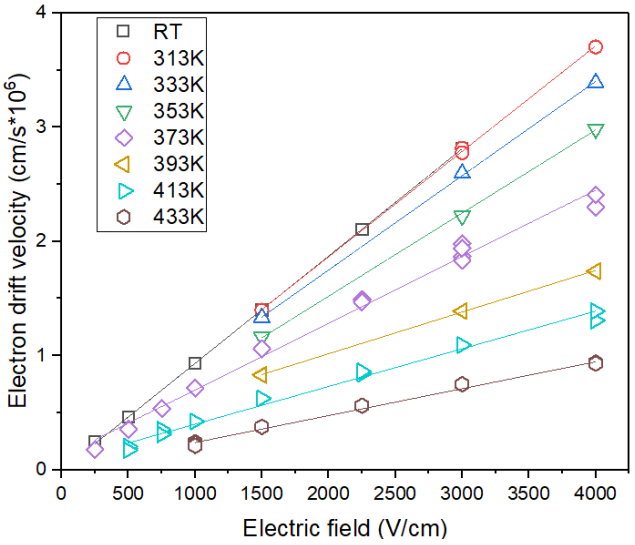

Figure 4.5. Experimentally measured electron drift velocities for different temperatures (T) as a function of the electric field (F).

ii. TOF of holes

Fig. 4.6 shows typical TOF signals due to the motion of holes for different light intensities. In general, TOF signal of holes closely resembles that measured for electrons. Indeed, at low light intensities, the TOF signal is quasi-rectangular, while becomes significantly distorted at higher light intensities, indicating that polarization largely depends on the charge concentration, rather than on the polarity of the drifting carriers.

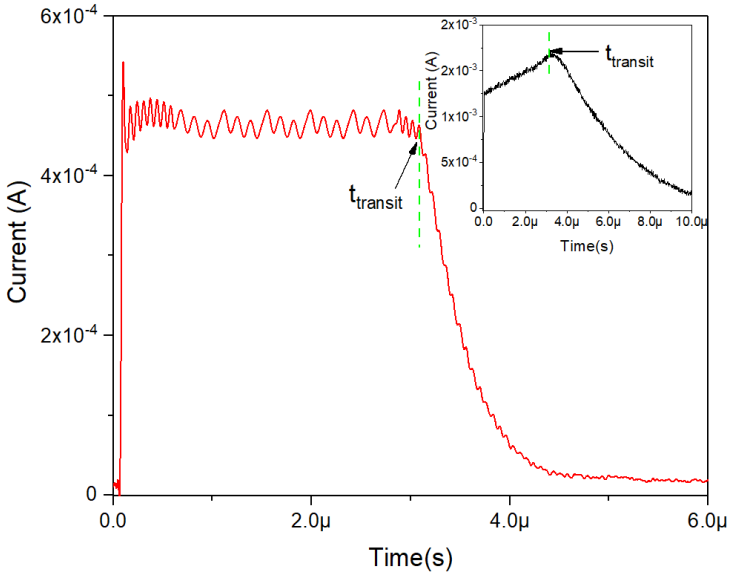

Figure 4.6. Typical time of flight signal for holes obtained at low and high laser intensity at 200 V bias. The inset to the figure shows the TOF signal measured at 15 x the initial light intensity.

Fig. 4.7 shows the temperature dependence of measured hole drift velocity on the applied electric field. The hole drift velocity increases linearly with the electric field, while it decreases with temperature.

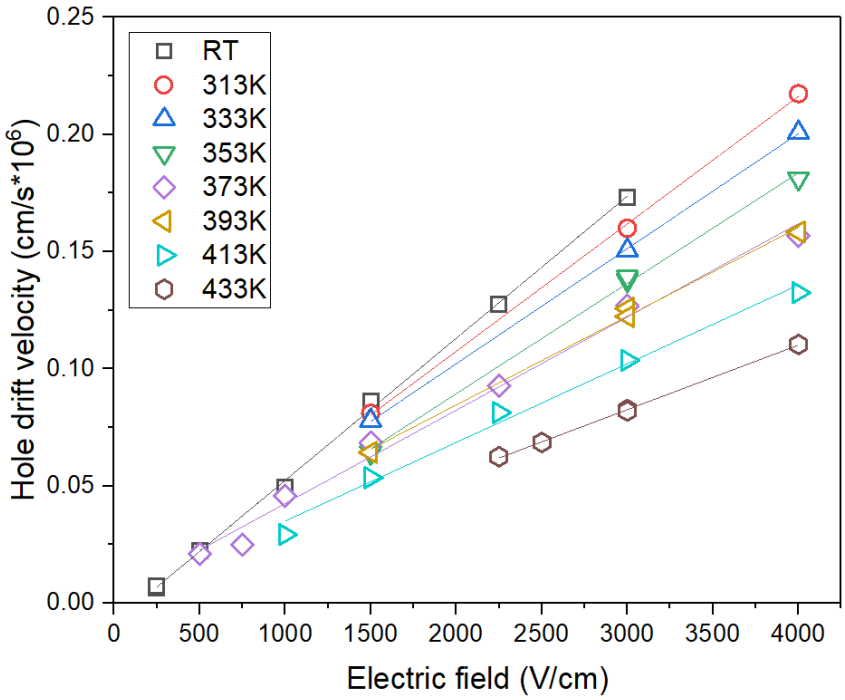

Figure 4.7. Experimentally measured hole drift velocities for different temperatures versus electric field.

The hole mobility, measured from the slopes of the drift velocities, also tends to decrease with temperature as shown in Fig. 4.8. As seen in Fig. 4.8, electron and hole mobilities both monotonically decrease with increasing temperature, while electrons are seen to be the faster carrier in CdZnTe at all temperatures. The electron mobility at 293 K was found $\mu_e = 939\ cm^2\ V^{-1}s^{-1}$, while hole mobility was only $\mu_h = 60\ cm^2\ V^{-1}s^{-1}$. At 433 K the electron mobility rolls-off to 235 $cm^2\ V^{-1}s^{-1}$ and hole mobility drops to μ_h = 27 $cm^2\ V^{-1}s^{-1}$ at the same temperature.

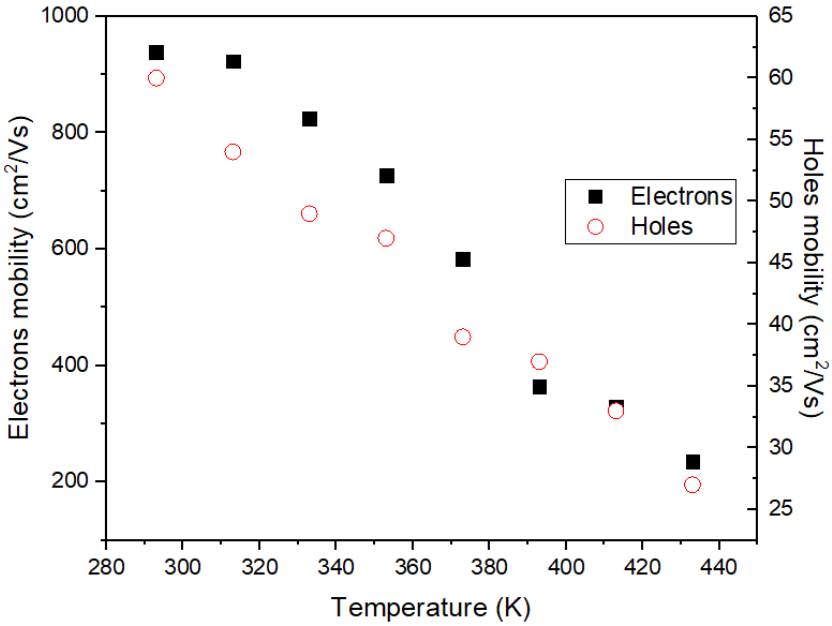

Figure 4.8. Temperature dependence of experimentally measured electron and hole mobilities.

It should be mentioned that after heating, the resistivity of sample #1 decreased by order of magnitude and previously obtained results on charge mobility were no longer reproducible. Although more research is needed, we believe that the contact stability was not maintained at higher temperatures. Since the properties of the sample #1 have changed, the low-temperature mobility measurements, which were conducted after heating are questionable and not shown here. Sample #2 was used for the further research.

b. Sample #2

i. TOF of electrons

Fig. 4.9 shows the TOF current transient for electrons at a selected bias of -800 V. In contrast to the TOF signal measured on sample #1, a gradual increase of the photocurrent over time was observed even at low light intensities, indicating that the electrons drift in a spatially-varying electric field. However, the electron transit time $t_{transit}$ can still be accurately determined from the well-defined peak in the TOF signal.

At higher light intensity (inset of Fig. 4.9), the shape of the TOF signal is further distorted and closely follows the behaviour of sample #1. The cusp, which corresponds to the transit time of the fastest carriers, occurs at ~0.8 x the transit time, measured at low light intensity, and agrees with the polarization model described elsewhere [58].

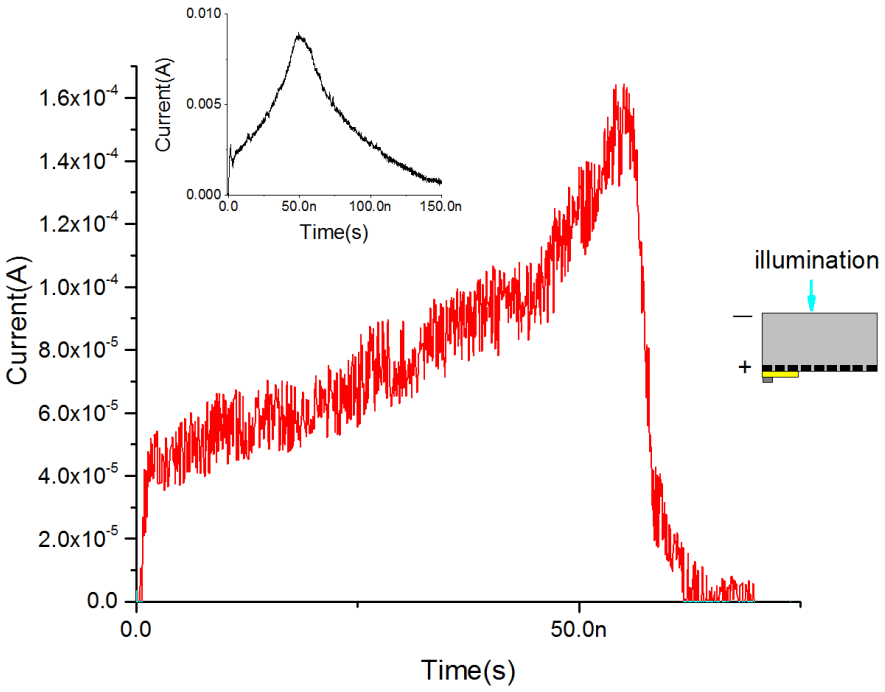

Figure 4.9. Typical TOF signal for electrons measured at -800 V applied to the continuous electrode.

Since, the electric field in the sample is inhomogeneous, the carrier drift velocity v should be determined as follows [59]:

$$\begin{cases} v(x) = \mu F(x) \\ v(x) = \dfrac{dx}{dt} \end{cases} \tag{4.1}$$

Subsequently, the drift mobility μ can be calculated as [59]:

$$\mu = \frac{1}{t_{transit}} \int_0^d \frac{dx}{F(x)} \tag{4.2}$$

where the distribution of electric field in the sample $F(x)$ can be calculated as [59]:

$$F(x) = \frac{j(t')d}{\mu \int_0^{\infty} j(t)dt} \tag{4.3}$$

where $j(t)$ is the photocurrent generated at the certain time t. In contrast to previously used Eq.1.2, 1.3, Eqns. 4.1 - 4.3 take into account the spatial distribution of the electric field in the sample but are very difficult to use in practice. On the other side, electron mobility, calculated with Eq. (4.2) yields a value of $\mu_e = 944$ cm^{2}V^{-1}s^{-1}, while the mobility

value, obtained with Eq. (1.3) resulted in electron mobility of μ = 930 $cm^{-2}V^{-1}s^{-1}$. Thus, the simplified calculation of the electron mobility with Eq. (1.3) produced only an insignificant error of 1.5% (which can be considered as a systematic error of the TOF). Therefore, Eq.1.2, 1.3 will be further used for drift velocity and mobility calculations with the error bar of 1.5%.

Fig. 4.10 shows the linear dependence of the electron drift velocity values on the applied bias for a wide range of temperatures from 193 K to 313 K with the upper value limited to ensure contact stability. Subsequently, the electron mobility values were derived from the slope of the drift velocity v_d. As seen in Fig. 4.10, both electron drift velocity and mobility decrease with temperature at fixed bias.

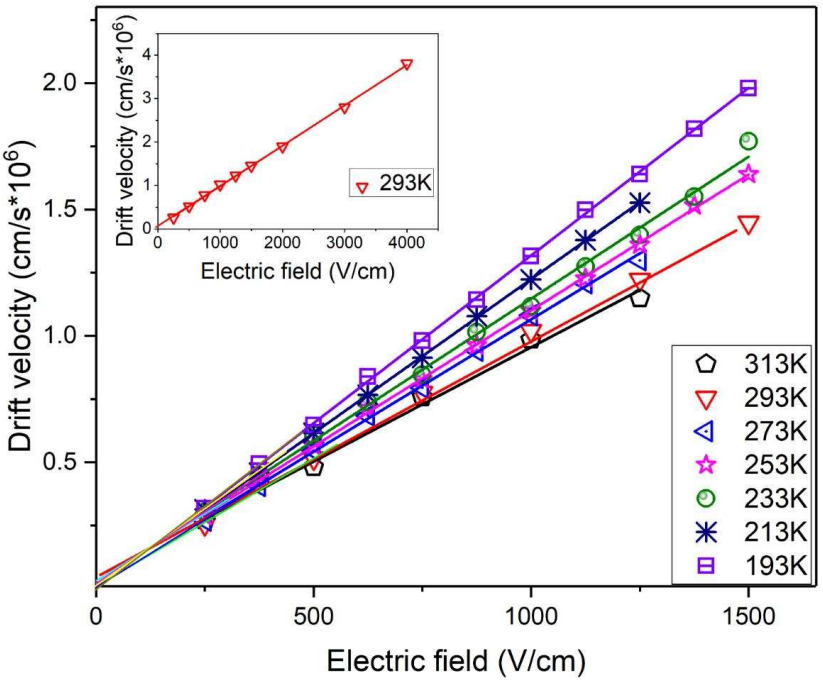

Figure 4.10. Experimentally measured electron drift velocities are plotted as a function of the electric field *(F)* for different temperatures *(T)*. The inset of the figure shows the electron drift velocity measured over a wider range of electric fields up to 4000 V/cm for the selected temperature T=293K.

ii. TOF of holes

Fig. 4.11 shows typical TOF signals due to the motion of holes when the sample is irradiated through the pixelated electrode. The hole photocurrent in CdZnTe sample #2 is also not quasi-rectangular, however in contrast to electron TOF signal, it decreases over time. The inset to Fig. 4.11 shows the TOF measurements performed with the ~15

times higher light intensity. Qualitatively, the difference between the TOF signals at low and high intensity is similar to that observed for electron transport: as intensity increases, the TOF transient develops a well defined cusp, indicative of a polarization effect.

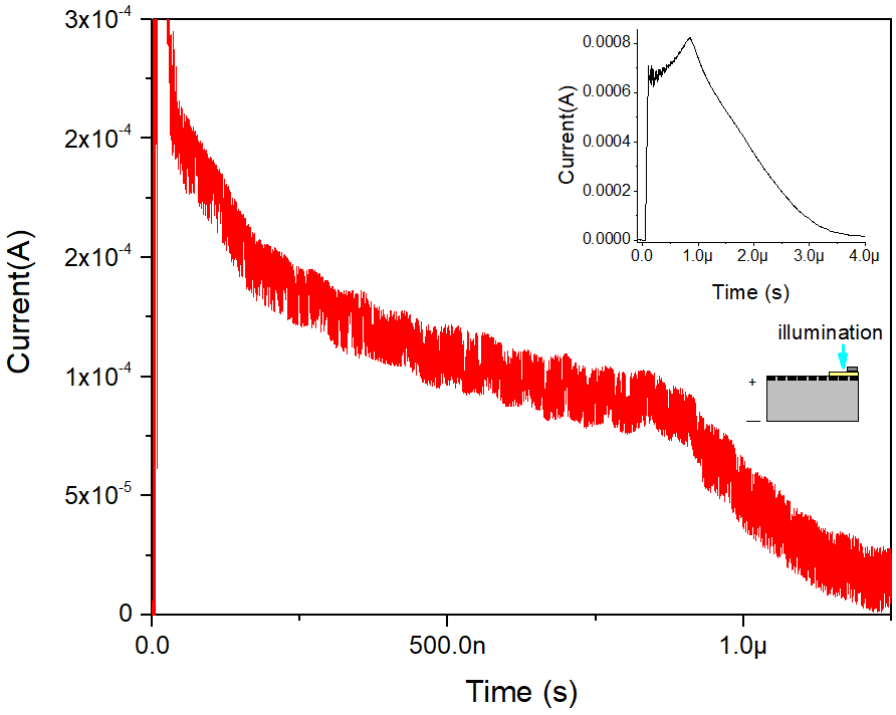

Figure 4.11. Typical time of flight signal for holes obtained for low (red curve) and high (black curve) laser energies from -800 V bias applied to the continuous electrode.

Fig. 4.12 shows the dependence of hole drift velocity on the applied electric field and temperature. The hole drift velocities were calculated from the transit time (defined by the knee of the TOF signal). Using Equations (1.3) and (4.2) resulted in a systematic error of 4.5%.

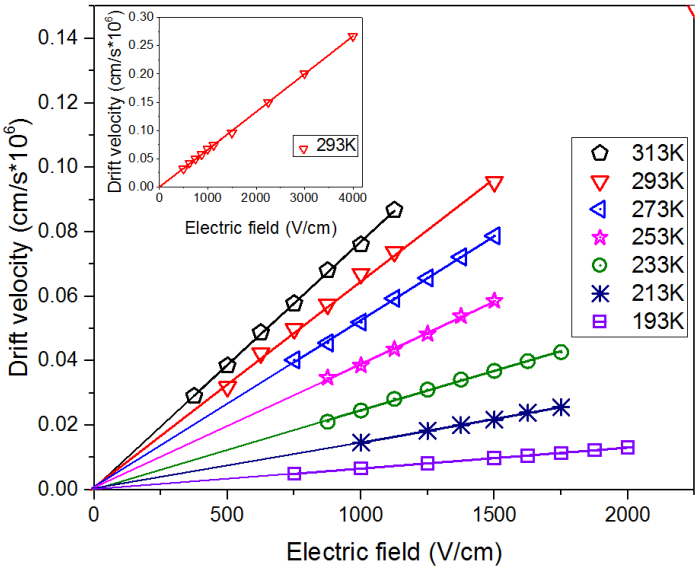

Figure 4.12. The hole drift velocities are plotted versus electric field for different temperatures. The inset of the figure shows the hole drift velocity, measured over a wider range of electric fields up to 4000 Vcm^{-1} for the selected temperature T = 293K.

Fig. 4.13 shows the temperature dependence of the electron (black squares) and hole (open red circles) mobilities measured from 193 K to 313 K. An increase in temperature causes holes drift mobility (and velocity) to increase from μ_h = 6.0±0.3 $cm^2V^{-1}s^{-1}$ at 193 K to μ_h = 79±4 $cm^{-2}V^{-1}s^{-1}$ at 313 K. The temperature behaviour of holes in CdZnTe is very different from that of electrons. Indeed, the electron mobility decreases with temperature from μ_e = 1350±20 $cm^{-2}V^{-1}s^{-1}$ at 193 K to 940±14 $cm^{-2}V^{-1}s^{-1}$at 313 K.

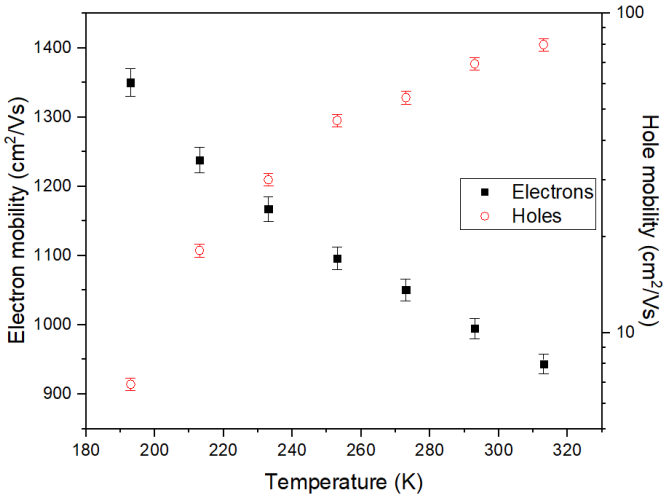

Figure 4.13. Temperature dependence of experimentally measured electron and hole mobility.

4.2.3 Discussion

a. Electric field inhomogeneity

The measured electron and hole mobilities for both CdZnTe samples measured here are very similar, however the temporal performance of the two samples is very different. The quasi-rectangular shape of the TOF signal, measured on sample #1, is indicative of the non-dispersive charge transport (i.e. charge carrier drift with constant mobility) in a constant electric field [31, 11]. In contrast, TOF signals measured on sample #2 indicate time-varying photocurrents, indicative of a inhomogeneous distribution of the electric field [60, 43].

Qualitatively, TOF transients of both types of carriers in sample #2 are mirror-symmetric: while the hole photocurrent decreases with time, the signal due to electron drift increases. In both cases the transient time is well defined, allowing accurate derivation of the drift velocities and mobilities. Normally, the deviation from the quasi-rectangular shape in the TOF signal profile suggests either the so-called dispersive mode of charge transport for which the carrier mobility decreases over the course of time, or a non-uniformity of the electric field inside the material (or the combination of two). Although a gradual decrease in the hole photocurrent with time can in principle be explained by dispersive transport, the increase in electron photocurrent strongly points to an electric field non-uniformity so that electrons face gradually increasing electric field while propagating through the sample. In contrast, holes facing a gradually decreasing electric field should be responsible for the shape of the photocurrent of holes.

Our results are quite similar to that observed by Suzuki et al. [42, 43, 11] and Uxa et al. [60]. Both authors related a re-distribution of the electric field to homogeneously distributed (constant) space charge within the CdZnTe, and used this assumption to determine an electric-field profile which appeared to be linear [42, 43, 60, 61]. In general, a charge-drift experiment (TOF) can sense any field distribution regardless whether the space charge is distributed uniformly or not. Following an approach suggested in Reference [59], we derived an internal field profile from the experimentally observed time dependences of the transient current using Eq. (4.3) (see Fig. 4.14).

As this is seen from Fig. 4.14, the internal electric filed changes nonlinearly within the sample. Therefore, the assumption of a homogeneous distribution of space charge is inapplicable to the studied CdZnTe sample #2 and it is more reasonable to assume that there are two distinct regions with different space charge densities. The transition between the two regions can be described using a Heaviside step function or a smooth function. To consider both cases, the space charge density was defined as [62]:

$$\rho(x) = q\left(N_1 + N_2 \frac{1}{1+e^{2k(x-x_0)}} \right) \tag{4.4}$$

where N_1, N_2 – charge concentrations, x_0 – a central point of the transition zone, q – an elementary charge, k – a parameter which determines the sharpness of the transition. The careful tuning of the fitting parameters x_0, N_1, N_2 and k allows for accurate investigation of the electric field inhomogeneity in the considered two-regional system.

Finally, an analytical solution for the electric potential in our CdZnTe sample can be found by solving the well-known Poisson equation:

$$\Delta\varphi = \frac{\rho(x)}{\varepsilon\varepsilon_0}, \tag{4.5}$$

where φ is the electric potential, $\rho(x)$- the space charge density provided by Eq. (4.4), ε - dielectric permittivity (ε =10.9 for CdZnTe [1]) and ε_0 is the permittivity in a vacuum. If the pixellated face of the sample is chosen as the origin of the coordinate system, then the boundary conditions can be written as:

$$\begin{cases} \varphi(0) = \varphi_0 \\ \varphi(d) = 0 \end{cases} \tag{4.6}$$

The solution of the Eq. (4.5) can be found by taking into account the charge density distribution described by Eq. (4.4) and the boundary conditions defined by Eq. (4.6) (see Appendix A) as:

$$\varphi(x) = -\frac{1}{4dk^2}\left\{ (d-x)\zeta(x) + N_2\theta\xi(x) \right\}, \tag{4.7}$$

where

$$\zeta(x) = 2k^2\left(\theta d\left(N_1 + N_2\right)x - 2\varphi_0\right) + \theta N_2\, Li_2\left(-e^{-2kx_0}\right),$$
$$\xi(x) = xLi_2\left(-e^{2k(d-x_0)}\right) - dLi_2\left(-e^{2k(x-x_0)}\right) \tag{4.8}$$

where $Li_\alpha(x)$ is a polylogarithmic function of the order α and $\theta = \frac{q}{\varepsilon\varepsilon_0}$. The distribution of the electric field in the sample can now be expressed as follows:

$$F(x) = -\nabla\varphi(x) \tag{4.9}$$

where ∇ is the nabla operator. Finally, substituting equation (4.7) into (4.9) gives:

$$F(x) = \frac{1}{4dk^2}\left\{2k\eta(x) + \theta N_2\left(Li_2\left(-e^{2k(d-x_0)}\right) - Li_2\left(-e^{2kx_0}\right)\right)\right\}, \tag{4.10}$$

where

$$\eta(x) = k\left(2\varphi_0 + \theta\left(N_1 + N_2\right)d\left(d - 2x\right)\right) + \theta d N_2 ln\left(1 + e^{2k(x-x_0)}\right) \tag{4.11}$$

Step-by-step derivation of the equation (4.10) can be found in Appendix B.

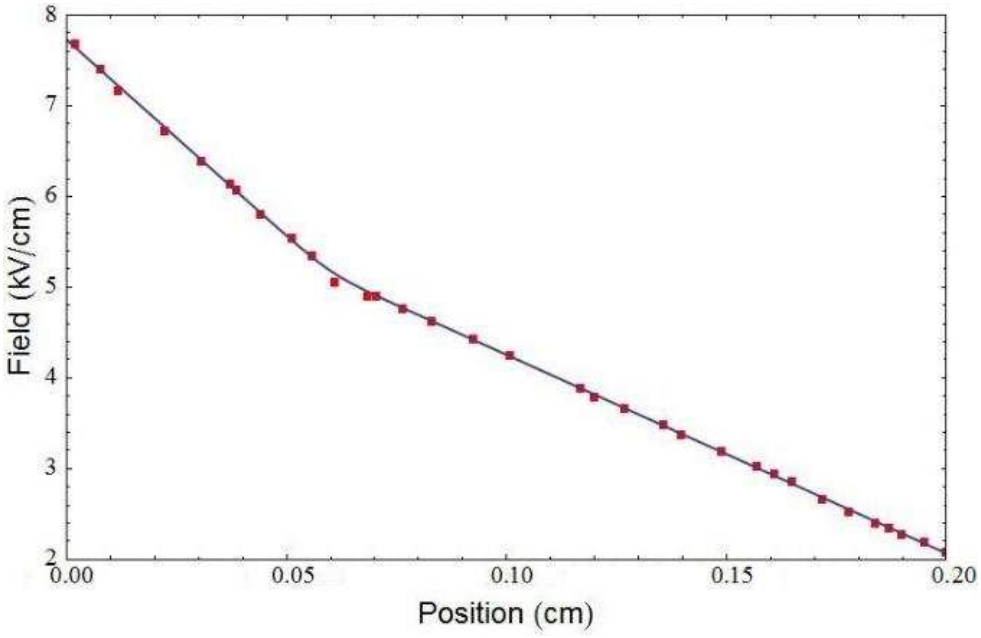

a)

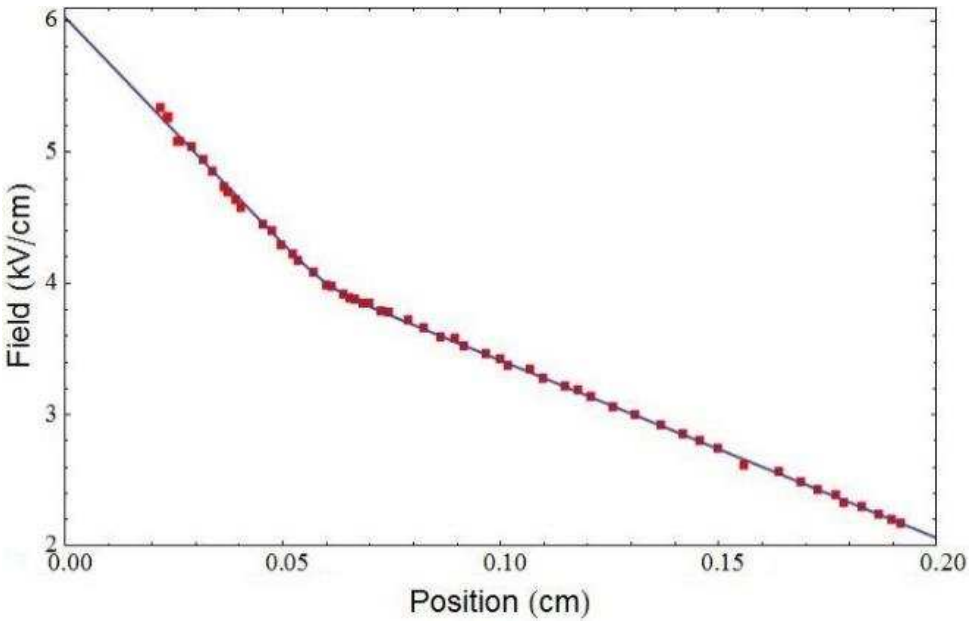

b)

Figure 4.14. Internal electric field distribution across the sample thickness (red squares) calculated from a) electron TOF current b) hole TOF current using Eq. (4.3). The blue line represents fitting function given by equation (4.10).

The fit of the electric field distributions obtained from the TOF current transients for electrons and holes by equation (4.10) is shown in Fig. 4.14. The fitting was done using the Wolfram Mathematica 11.1 software package with the fitting parameters listed in Table 4.2. It should be noted that the above theory is not limited to a two-region space charge distribution and can be expanded to a multiple-region case. The calculation of electric potential and the internal electric field distribution for the case of M regions is provided in Appendix B.

Table 4.2 Electrons and holes fitting parameters

Parameter	Holes	Electrons
N_1 x10^{10}, [cm^{-3}]	8.15	13.2
N_2 x10^{10}, [cm^{-3}]	12.7	12.9
k, [cm-1]	14900	14900
φ_0, [V]	721	890
x_0, [cm]	0.06	0.06

As seen from Fig. 4.14 and Table 4.2, the same "two-region" inhomogeneity of the electric field is responsible for the shape of the TOF signals for both electrons and holes. The drifting carriers experience an electric field enhancement in the 0.6 mm region from the pixelated electrode due to the larger concentration of space charge there. It should be noted that the fitting parameters, listed in Table 4.2 are very similar for electrons and holes, except for the values of the carrier concentrations N_1 (8.15 x10^{10} cm^{-3} for electrons versus 13.2 x10^{10} cm^{-3} for holes). In addition, the electron photocurrent increases steeper than that for holes in the field enhancement region (see Figs. 4.11, 4.9), suggesting that the photogeneration of electrons produces an extra charge accumulation, when measured under the same conditions (light intensity, electric field). Although more investigation is needed to explain this effect, the plausible explanation might be a photoconductive gain which is triggered, when the charge carriers are photo-generated from the continuous electrode side. Since we suspect that the electron space charge density might be affected by the photoconductive gain, the fitting parameters for holes from Table 4.2 were used to plot the coordinate dependencies of the space charge density, electric field, and the electric potential in our CdZnTe sample, shown in Fig. 4.15. The inset of the Fig. 4.15a shows the transition area between two regions which was found to be $d_w \approx 6.7\mu m$.

Overall, our results on the space charge density agree well (by order of magnitude) with the numbers reported in [42, 43, 60, 61]. However, our approach allows

for more detailed evaluation of the electric field inhomogeneity than in previous studies. Indeed, contrary to the theory used by others [43, 60, 61], in our model the Poisson equation was solved without an assumption of homogeneity of the space charge density distribution throughout the sample thickness and as such, our approach is not limited by uniformly distributed space charge and can be used to account for any particular distribution.

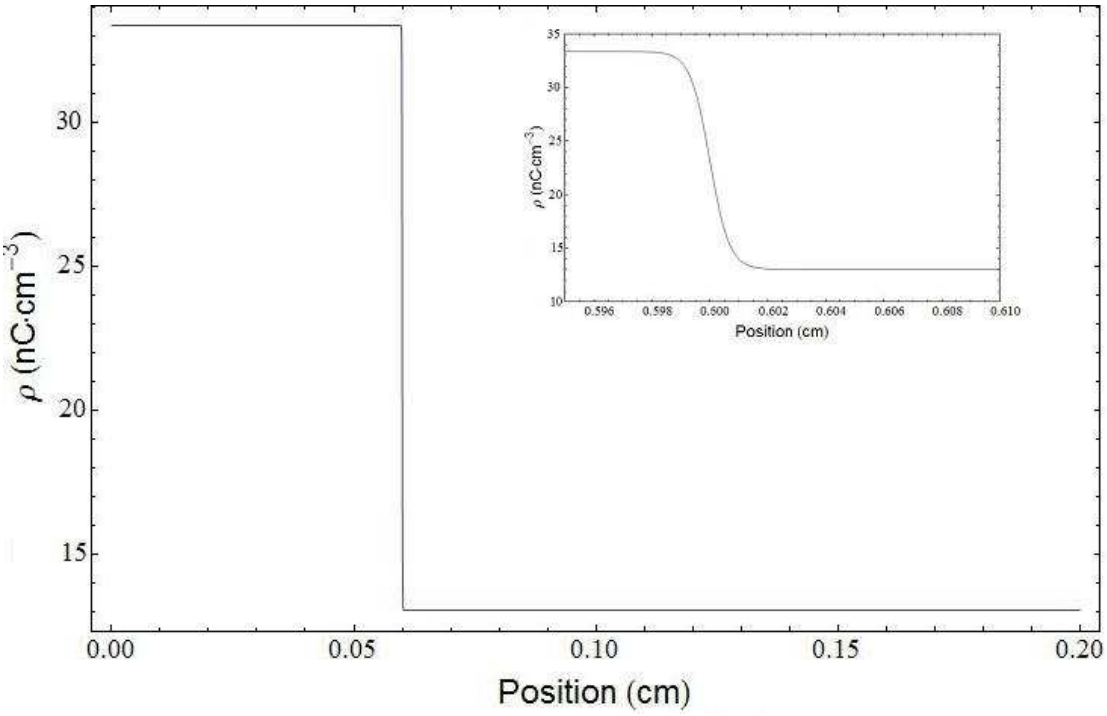

a)

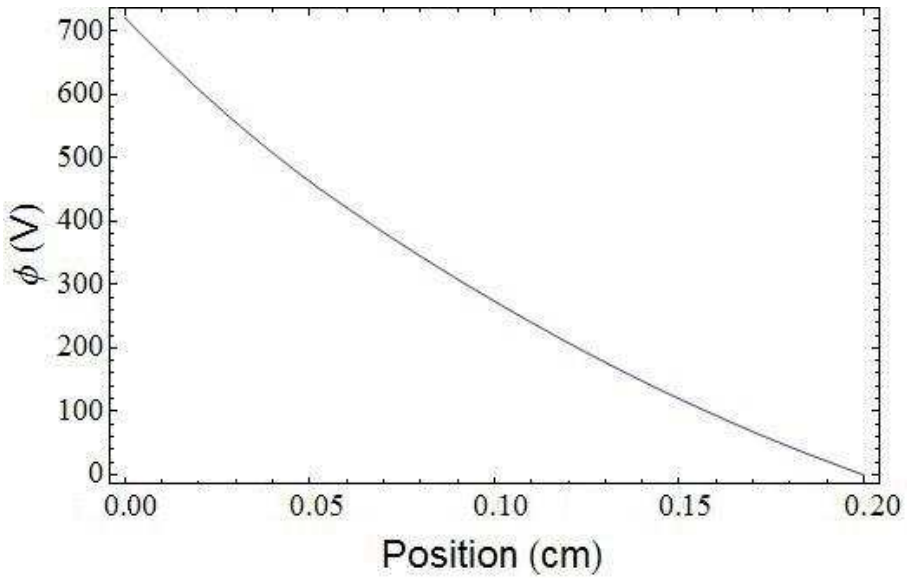

b)

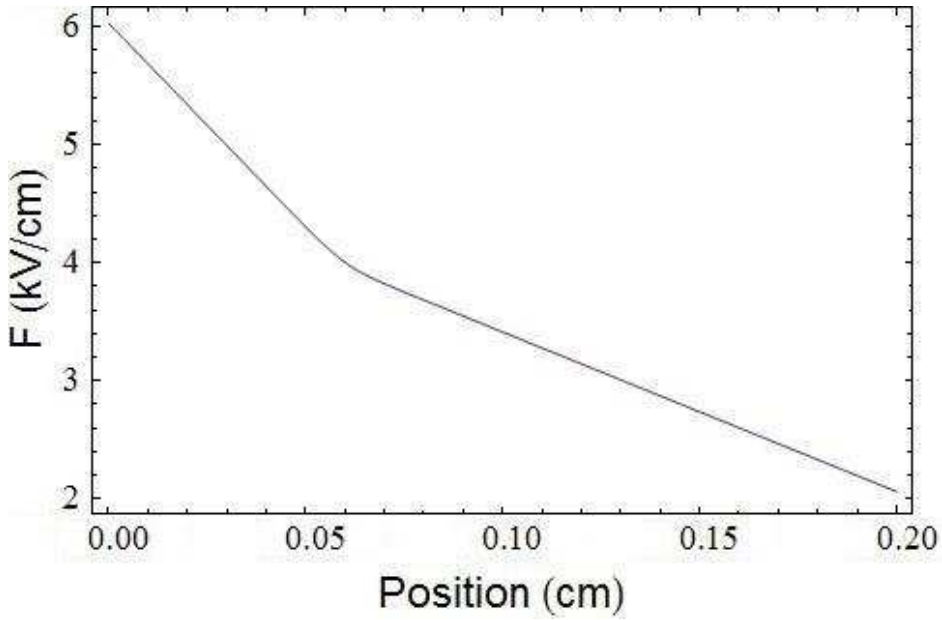

c)

Figure 4.15. Coordinate dependencies of a) space charge density $\rho(x)$ b) elctric potential, c) electric field in the studied CdZnTe sample. The inset to a) shows the magnified view of transition between two concentration levels

b. Temperature dependencies of carrier mobilities

At room temperature, the electron drift mobility μ_e was found to be 944±14 $cm^2V^{-1}s^{-1}$, which is comparable to results obtained by previous investigators on high-grade CdZnTe crystals [60, 11]. The decrease in mobility with temperature is indicative of phonon scattering. However, fitting the experimentally measured values of electron mobility with a phonon scattering model described in Ref. [63], did not yield a good fit (see Fig. 4.16). Hence the analysis of the temperature dependence of the mobility was performed assuming that several scattering mechanisms contribute simultaneously, namely, phonon scattering, as well as scattering at both, ionized and neutral impurities:

$$\frac{1}{\mu^e_{total}} = \frac{1}{\mu^e_i} + \frac{1}{\mu^e_p} + \frac{1}{\mu^e_n} \tag{4.12}$$

where μ^e_p is the mobility due to phonon scattering given by [63]:

$$\mu^e_p = AT^S \tag{4.13}$$

μ^e_n is a temperature independent mobility due to the neutral impurity scattering [64] given by:

$$\mu^e_n = \frac{\pi^2 m^*_e q^3}{10\varepsilon_0 \varepsilon N_N h^3} \tag{4.14}$$

and μ^e_i is the mobility due to ionized impurity scattering [64] given by:

$$\mu^e_i = \frac{64\sqrt{\pi}\,\varepsilon_0^2 \varepsilon^2 \left(2k_B T\right)^{3/2}}{N_i q^2 \sqrt{m^*_e} \ln\left[1 + \left(12\pi\varepsilon_0 \varepsilon k_B T / q^2 N_i^{1/3}\right)^2\right]} \tag{4.15}$$

where A and S are temperature independent constants, m^*_e is the electron effective mass, h is the Planck constant, T is the temperature, k_B is the Boltzmann constant, N_i is the ionized impurity concentration (fitting parameter), and N_N is the concentration of neutral impurities (fitting parameter).

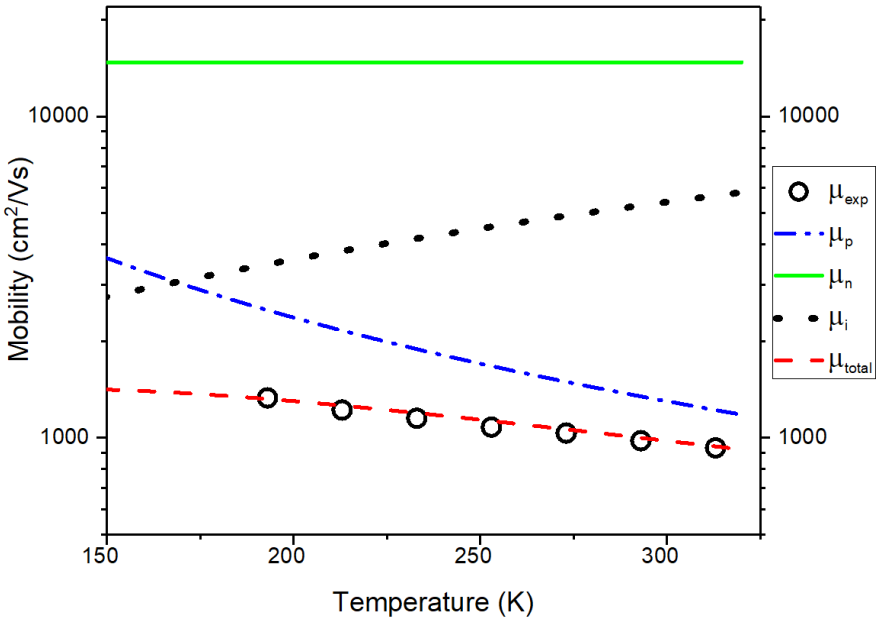

Figure 4.16. Temperature dependence of experimentally measured (black open circles) electron mobility. The contribution of several scattering mechanisms: phonon scattering (μ_p), neutral impurities (μ_n) and ionized impurities (μ_i). μ overall represents the fitted overall electron mobility. The size of the error bars is smaller than the size of the open circles.

As it can be seen from Fig. 4.16, that an excellent agreement between the measured and the calculated results are obtained. The fitting, yielded $m_e^* = 0.112m_0$ [11] and S = -3/2 [63, 65], and revealed the concentration of the ionized and neutral impurities to be 2.5x10^{17} and 10^{16} cm^{-3}, respectively. As seen from Fig. 4.16, the dominant processes are phonon scattering and scattering at ionized impurities, while neutral impurities have minimal effect on the electron transport. The obtained impurity concentrations are very similar to those published by others with the only difference the number of ionized impurities: 2.5x10^{17} cm^{-3} in our case in contrast to 2x10^{17} cm^{-3} published in [11]. The larger concentration of ionized impurities found here led to slightly smaller mobilities: 944±14 $cm^2V^{-1}s^{-1}$at room temperature verses 960 $cm^2V^{-1}s^{-1}$ in [11].

In contrast to electrons, a very different mechanism is responsible for hole transport. Indeed, the increase in hole mobility with temperature indicates that a multiple-trapping mechanism governs the holes in CdZnTe, and the hole drift mobility defined by Eq. (1.5). The multiple-trapping mechanism is a thermally activated process, characterized by:

$$\tau_r \sim e^{\frac{E_a}{k_B T}} \tag{4.16}$$

where E_a is activation energy [35]. The hole activation energy, de-trapping time constant and microscopic mobility were found to be $E_a = 0.13$eV, $\tau_t = 167$ ps and $\mu_0 = 148$ cm^{2}V^{-1}s^{-1}, respectively, by fitting the temperature dependence of hole mobility with Eqns. (1.5, 4.16) as shown in Fig. 4.17.

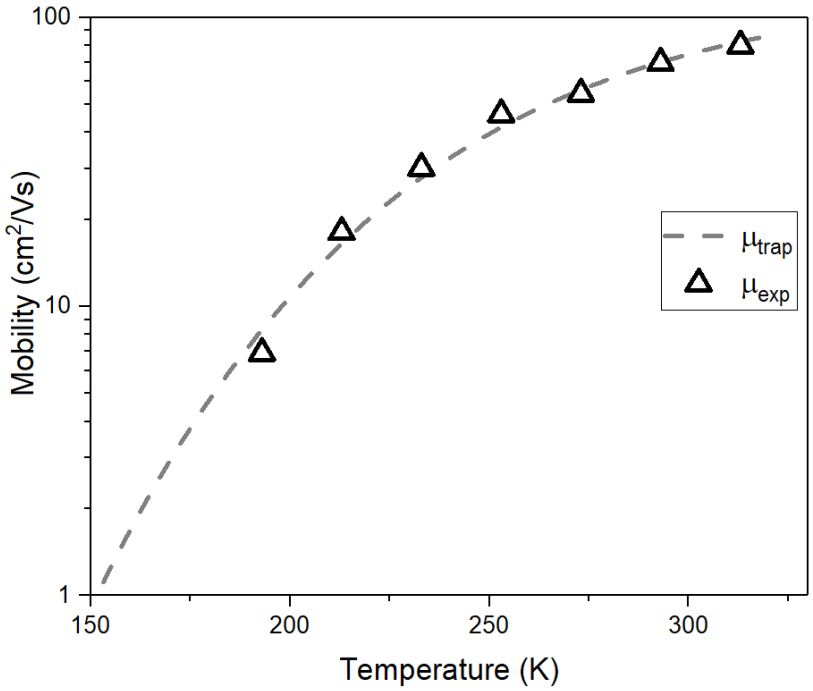

Figure 4.17. Temperature dependence of experimentally measured hole mobility. The uncertainty in the hole mobility is smaller than the size of the open triangles.

As can be seen in Fig. 4.17, the hole mobility tends to saturate slightly above 320 K, while multiple studies have shown that beyond 320 K, holes in CdZnTe do not undergo trapping [11, 66]. The comparatively high mobility values and small activation energy, suggest that at room temperature, hole mobilities are governed by shallow trapping rather than by dispersive nature of charge transport.

4.3 Charge Extraction by Linearly Increasing Voltage

In the early 2000's an alternative to TOF technique, called photo-charge extraction by linearly increasing voltage (photo-CELIV) was proposed [67]. In contrast to TOF, in photo-CELIV the non-equilibrium charge carriers are photo-generated in an unbiased sample. After a preset delay time, a linearly increasing voltage ramp is applied to the

sample to extract the generated charge. As the voltage increases, more carriers are extracted and the photocurrent rises. When most of the carriers are extracted, the photocurrent decays. Mobility is derived from the time needed to reach the peak of the photocurrent. In addition, when CELIV is measured in the dark (without the light pulse) it provides information on the accumulation of equilibrium charge carriers.

4.3.1 Experimental apparatus

Fig. 4.18 shows the schematic diagram of the photo-CELIV setup. The same laser as used for the TOF measurements (λ = 430 nm, pulse duration 35ps) was used to generate carriers at the surface of the unbiased sample. After 1 μs delay time a linearly increasing voltage ramp $A=U/t_{pulse}$ was applied to extract the photogenerated charge carriers. A Tektronix TDS 2024C oscilloscope with 200 MHz bandwidth and 10 kΩ parallel resistance was used to record CELIV photocurrent transients.

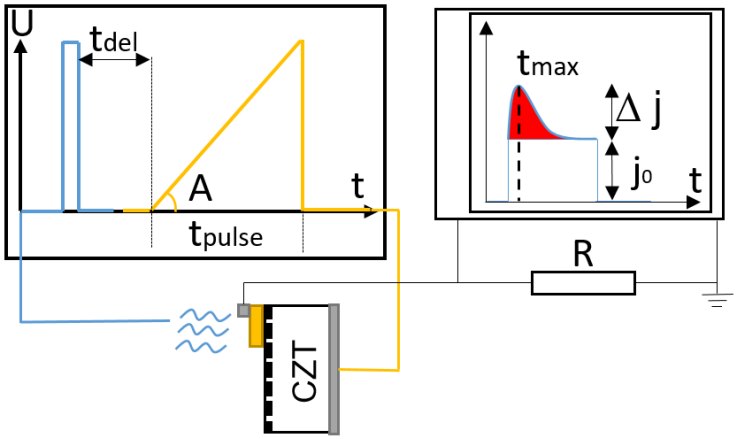

Figure 4.18. Schematic diagram of the photo-CELIV apparatus. The voltage from a generator is applied to the solid metal electrode. The extraction of equilibrium carriers (dark-CELIV) is performed without a laser pulse.

As shown in Fig. 4.18, the photo-CELIV signal consists of the constant capacitive displacement current j_0 due to the high voltage (HV), and the photocurrent Δj (shown in red). To estimate the carrier mobility from the CELIV measurements three cases should be considered [68]:

1. $\Delta j < j_0$ (low conductivity case). The charge carrier mobility can be calculated by t_{max} from CELIV transient as:

$$\mu = K\frac{d^2}{At_{\max}^2}, \tag{4.17}$$

where t_{max} is the time the current reaches the peak value, d is the sample thickness, A is the voltage ramp, K is a constant (K=2 for surface carrier generation and K=2/3 for bulk generation).

2. $\Delta j > j_0$ (high conductivity case). The charge carrier mobility can be estimated as:

$$\mu = \frac{d^2 j_0}{At_{\max}^2 \Delta j}, \tag{4.18}$$

3. $\Delta j \approx j_0$ (moderate conductivity case). Then mobility of the charge carriers is given by:

$$\mu = K\frac{d^2}{At_{\max}^2 B}, \tag{4.19}$$

where $B = 1 + \frac{0.36\Delta j}{j_0}$ is the correction factor.

CELIV measurements were also performed in the dark (termed as "dark-CELIV") to analyze mobilities of the equilibrium carriers. The results are presented in the next 2 subsections.

4.3.2 Results

Fig. 4.19a shows the typical photo-CELIV signal measured on CdZnTe sample #2. A clear photo-peak at t_{max} is seen on the CELIV trace (red line). The photocurrent increases rapidly with the linearly increasing voltage until the majority of mobile carriers are extracted at t_{max}, and then monotonously drops to the capacitive level. The magnitude of the photocurrent Δj has never exceeded the capacitive signal j_0. According to Ref. [68], when $\Delta j < j_0$ (as in our case), the charge carrier mobility should be calculated with Eq. 4.17. The obtained mobility values closely resemble those, measured with TOF (see Fig. 4.13).

It should be noted, that when CELIV measurements were performed in the dark (black line in Fig. 4.19a), the extraction peak was smaller, but no distinguishable shift in t_{max} between the dark and photo-CELIV has been observed. The charge mobility, derived from this peak, corresponded to hole mobility, measured with photo-CELIV (~62 $cm^2V^{-1}s^{-1}$). The total extracted charge in the dark-CELIV signal was found to be several orders of magnitude smaller than the *CV* charge, accumulated on the bias electrodes, under normal detector operation conditions. The dark-CELIV measurements were repeated at elevated temperatures in an attempt to release the charge from the reservoir (i.e. from the charge accumulation region). However, increasing the temperature to 60 °C (limited by the electrode stability) didn't show any effect. Interestingly, when positive polarity was applied in the dark (Fig. 4.19b), a linearly increasing signal was observed without a clear extraction peak. The signal increase, shown in Fig. 4.19b, corresponds to a dark current of ~55 nA at 200 V bias in good agreement with direct measurements of sample resistivity.

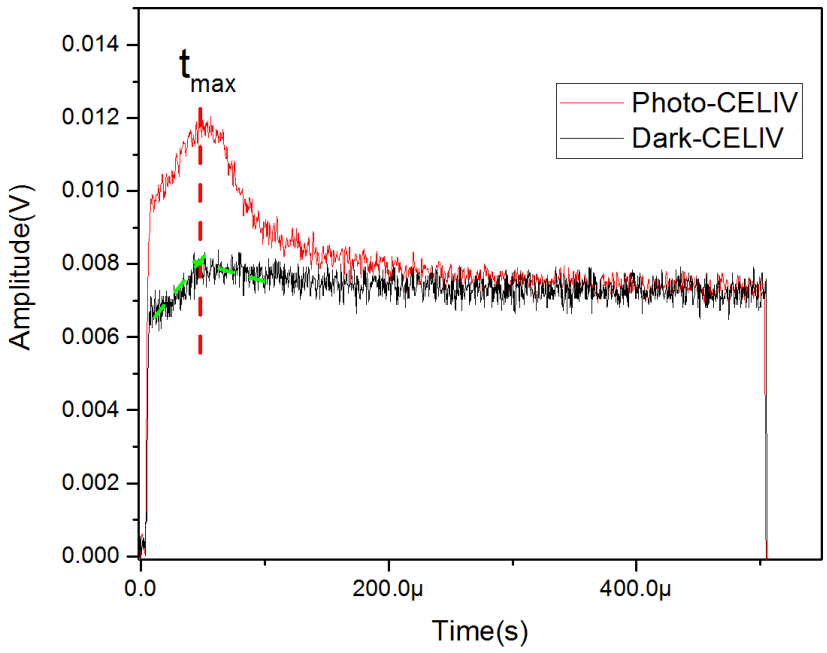

a)

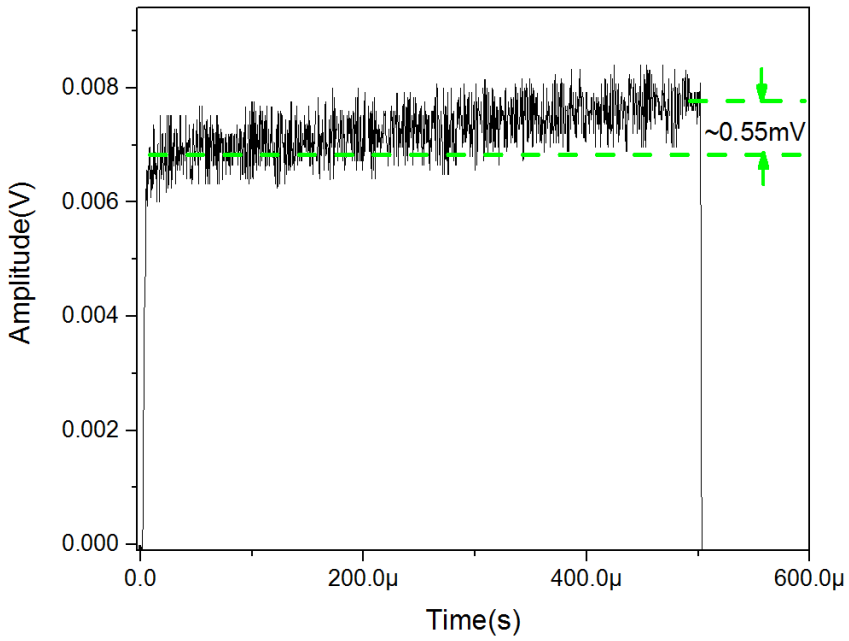

b)

Figure 4.19. a) Dark-CELIV (black) and photo-CELIV (red) signal at -200 V b) Dark-CELIV transient at +200 V. Note: bias is applied to the continuous electrode.

4.3.3 Discussion

The photo-CELIV measurements of charge mobility in CdZnTe sample #2 have confirmed the values, previously found with TOF. However, the dark-CELIV experiments revealed an interesting feature, missed by the TOF, namely, the presence of a charge reservoir in the sample, evident from the drastic difference between dark-CELIV transients (see Figs.4.19 a,b). The charge extraction from such a reservoir is observed only when the positive polarity is applied to the pixelated electrode. This suggests that the reservoir is filled with the trapped holes (rather than an electron), which are released with the application of an electric field. In addition, the mobility of charge carriers, extracted from the reservoir coincides with the photogenerated hole mobility in CdZnTe. The location of the reservoir might be determined by comparing the dark and photo-CELIV signals. If it was located in the bulk of the sample, the equilibrium carriers would drift a shorter distance than their counterparts, photogenerated by strongly absorbed light near the illumination electrode interface. This would result a shorter t_{max} of the dark CELIV signal. However, the extraction maximums of the dark and photo-CELIV signals coincide, indicating that hole reservoir is located close to the pixelated electrode-CdZnTe

interface. It should be noted, that since raising temperature has shown no effect on the reservoir, it indicates that holes are captured at relatively deeply-lying trapping states. Although the presence of such a reservoir is undesirable, the total charge contained in it is too small (much smaller than *CV*) to produce any detectable effect on detector performance (i.e. to re-distribute the internal electric field).

4.4 Pulse Height Spectroscopy (PHS)

As was mentioned in section 1.4, PHS with monoenergetic x-ray excitation is one of the key methods to investigate the mobility-lifetime product ($\mu\tau$) in photoconductors. In addition, it provides insight into the charge photogeneration processes and in particular it allows determiation of the average energy required to generate a single electron-hole pair $W_{\pm}$. $W_{\pm}$ is one of the most important performance parameters for photoconductors used as radiation sensors since it defines the sensitivity to x-rays. Moreover, since the signal is generated by a single absorbed x-ray photon, it does not lead to an electric field redistribution inside the sample [69], which is particularly important for CdZnTe investigation (see section 4.2).

4.4.1 Experimental apparatus

Fig. 4.20 shows a typical PHS apparatus. For PHS measurements, the charge carriers were generated by 59.5 keV x-ray photons, emitted by an ^{241}Am source, while a constant bias was applied to the sample. For our sample thickness (2 mm), the probability of photoelectric interaction at photon energy ε = 59.5 keV for CdZnTe is ~95% [70] (Fig. 2.10), suggesting full absorption of the incident photon energy. The signal was read out from the pixelated electrode face with a custom-made preamplifier, then coupled to a pulse shaping amplifier (APTEC 6300). A multi-channel analyzer MCA, Ortec ASPEC927 was used to discriminate the amplified signals by energy. A negative polarity was applied to the continuous electrode for all experiments since it provided the lower dark current values (Table 4.1). Calibration of the PHS setup was performed by a Si PIN photodiode (Thorlabs, model FDS010) with a $W_{\pm}$ value of 3.62 eV/ehp [32].

In order to prevent the pulse pile-up a relatively weak radioactive source was used, which provided a count rate ~100 s^{-1}. The effect of the ballistic deficit (i.e.

incomplete charge collection caused by the shaping time smaller than the transit time) was minimized by setting shaping time τ_s of the amplifier to be equal or slightly larger than the transit time of charge carriers, derived from TOF measurements (see section 4.2). Thus, τ_s was varied from 50 ns to 5 µs, depending on the polarity of the drifting carrier. The measurements were conducted in electric field range spanning the typical CdZnTe operating field of 4000 Vcm^{-1}, i.e., from 3000 Vcm^{-1} to 5000 Vcm^{-1} with a step of 1000 Vcm^{-1}. The absorption depth of 2 mm thick CdZnTe for the same energy (59.5 keV) is around $\delta \approx 250$ µm [49, 70] meaning that majority of electron-hole pairs were created close to CdZnTe surface. Thus, transport properties of each type of carriers can be investigated individually by changing the irradiation face [39].

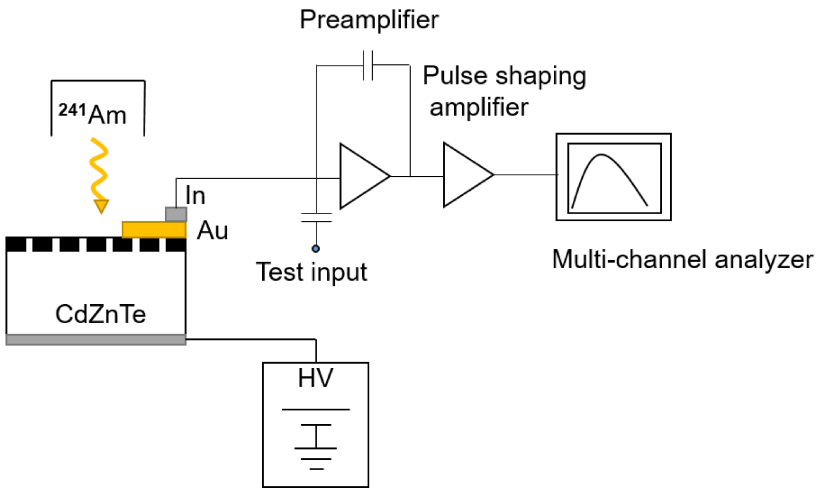

Figure 4.20. Schematic representation of the pulse height spectroscopy setup.

4.4.2 Results

a. PHS of electrons

Fig. 4.21 shows a calibrated pulse height spectrum of electrons in CdZnTe, measured with the cathode facing the x-ray source. For this measurements, the energy discrimination was set to ~8300 EHP in order to filter noise due to absorption of scattered photons and other low energy photons emitted by the ^{241}Am source. The spectral waveform is seen is nearly Gaussian with an absorption peak well separated from the background noise.

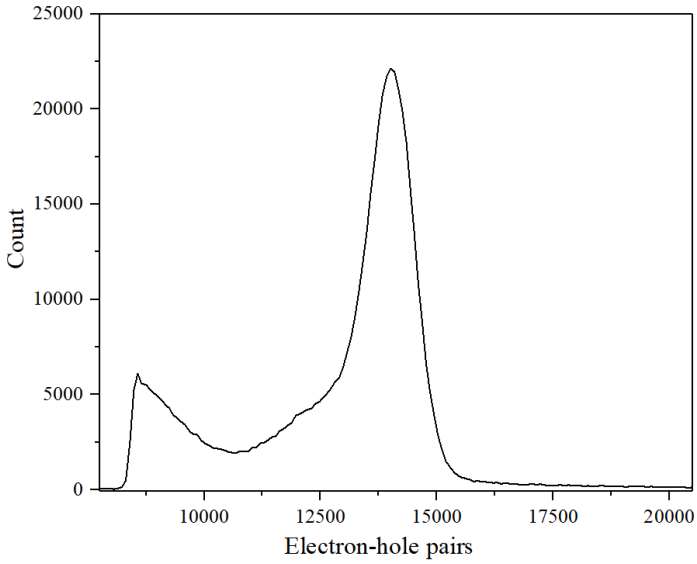

Figure 4.21. Pulse height spectrum measured on a 2 mm CdZnTe sample at F = -3000Vcm^{-1} applied to the solid metal electrode, $\varepsilon = 59.5\ keV$, $\tau_s = 100\ ns$. The cathode is facing the x-ray source.

In order to check for the ballistic deficit, the PHS measurements were performed for different τ_s for the selected F = 3000Vcm^{-1} as shown in Fig. 4.22. The majority of the charge is collected within 100 ns, which agrees very well with the electron transit time at this F. Further increase in τ_s provides a marginal increase of the collected charge, therefore a shaping time $\tau_s = 100$ ns was chosen for all electron charge collection measurements.

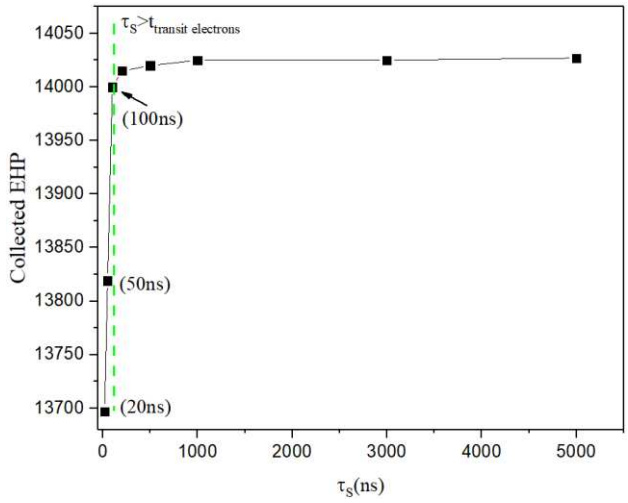

Figure 4.22. Collected charge as a function of τ_s for electrons at F = -3000Vcm^{-1}.

Fig. 4.23 shows the electron pulse-height spectra obtained for different electric fields and the shaping time set to $\tau_s = 100$ ns. A negligibly small shift of the spectral peak position Q_0 (corresponding to the total charge collected) to the right with increasing electric field was observed. $W_{\pm}$ values were derived from the spectral peak position and the energy of the X-ray photon ε as:

$$W_{\pm} = \frac{\varepsilon}{Q_0} \tag{4.20}$$

and plotted as a function of F in Fig. 4.24.

In addition, charge collection efficiency (*CCE*) of the detector, measured as the ratio of the theoretical W_{theor} = 4.2 eV/ehp [71] to the measured one ($CCE = W_{theor}/W_{\pm}$), is also shown in Fig. 4.24. The measured $W_{\pm} \approx 4.21$ eV/ehp at F = 3000 Vcm^{-1} and is seen to be almost electric field independent, while *CCE* of the detector is nearly 100%.

The mobility-lifetime product $\mu\tau$ is traditionally evaluated by fitting the $W_{\pm}$ dependence on the applied bias with the depth-dependent Hecht equation (Eq.1.4) [33, 8]. However, in our case, with only one type of charge carrier (electrons) contributing to the signal, it allows us to use a simplified equation (1.6) [39]. Fig. 4.24 shows the fit of $W_{\pm}$ values with the simplified Hecht equation (1.6), which revealed $\mu_e\tau_e = 3.5\times10^{-3}$cm^2/V.

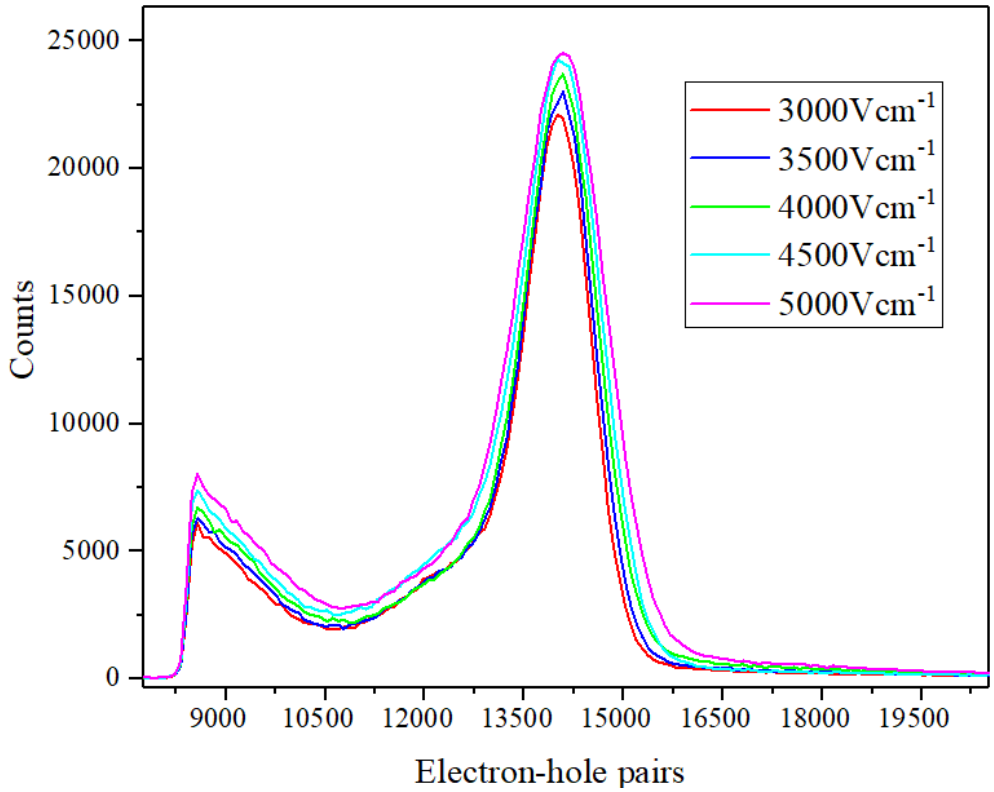

Figure 4.23. Electrons pulse height spectrum obtained with different voltages applied to the solid electrode (from -3000Vcm^{-1} up to -5000Vcm^{-1}).

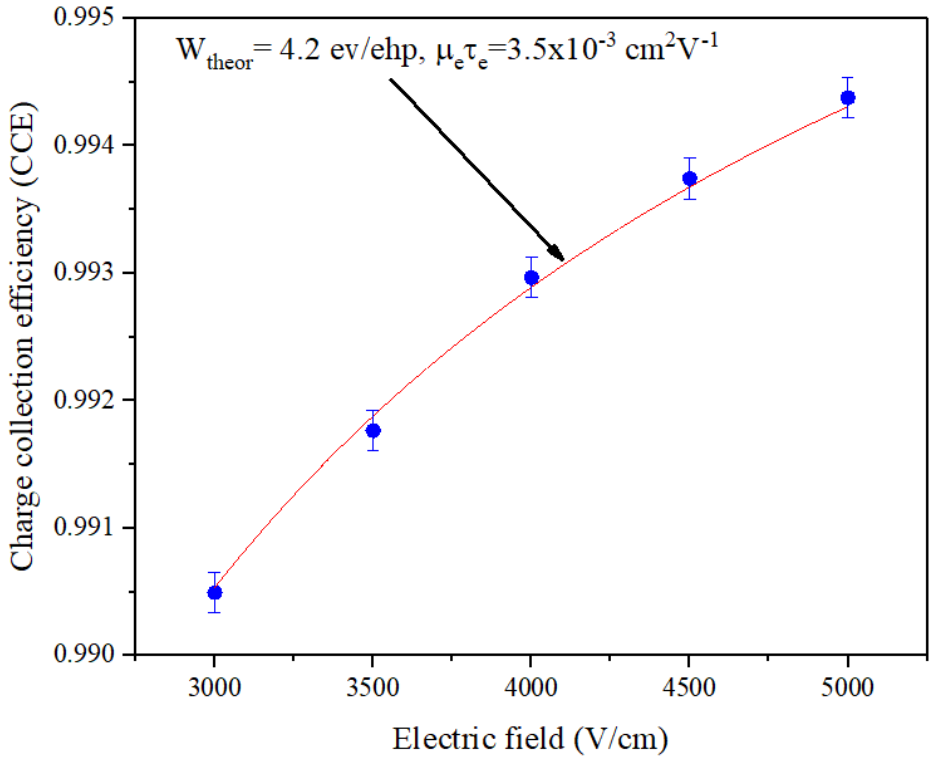

Figure 4.24. Charge collection efficiency (*CCE*) as a function of electric field for electron PHS. The blue circles represent the experimental results while the red line shows the simplified Hecht fit.

b. PHS of holes

The hole transport in CdZnTe was investigated by moving the ^{241}Am source to face the pixelated electrode side, while the polarity of the applied bias remained the same. Fig. 4.25 shows the pulse-height spectrum of holes at F = -3000Vcm^{-1}. The spectrum has a Gaussian shape with a well-defined peak corresponding to the absorption of 59.5 keV x-ray photons. In order to check for the ballistic deficit, the PHS measurements were performed at different shaping times. Fig. 4.26 shows Q_0 as a function of τ_s for the case of F = -3000 Vcm^{-1}. Majority of holes are seen to be collected within 1 μs, which was set to be the shaping time for all further experiments.

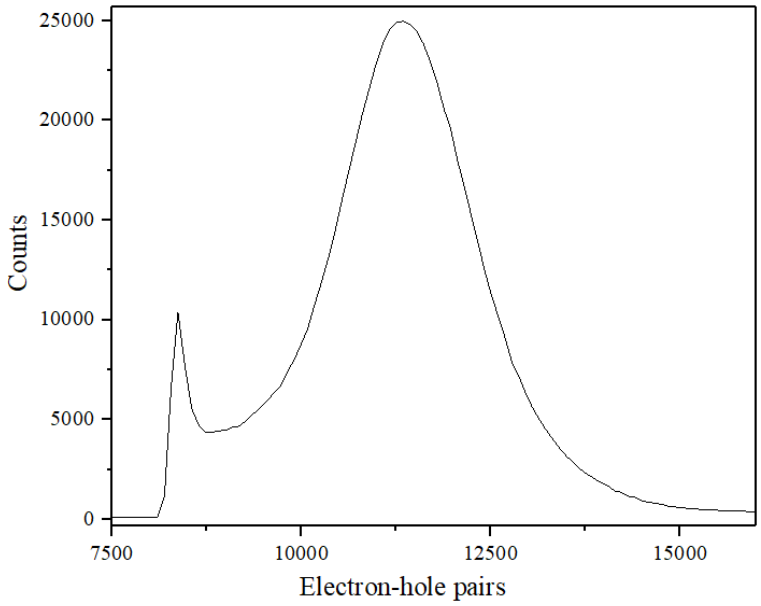

Figure 4.25. Pulse height spectrum measured with 2 mm CdZnTe sample at F = -300Vmm^{-1} applied to the solid metal electrode, $\varepsilon = 59.5\ keV$, $\tau = 1\ \mu s$. The anode is facing the x-ray source.

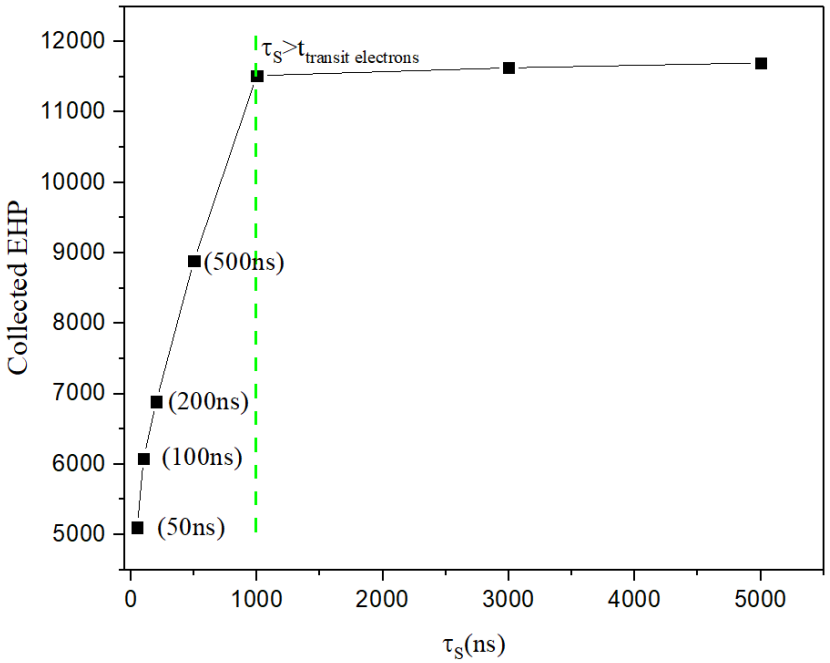

Figure 4.26. Collected charge as a function of τ_s (amplifier shaping time) for holes at F = -3000Vcm^{-1}.

Fig. 4.27 shows the pulse height spectra measured at $\tau = 1\ \mu s$ for F, between -3000 Vcm^{-1} and -5000Vcm^{-1}. The spectral peak Q_0 is seen to shift to the right with a higher electric field, reaching a value of Q_0 ~ 12500 ehp at F = -5000Vcm^{-1}.

Fig. 4.28 shows the dependence of $W_{\pm h}$ on F, calculated with Eq. (4.20). $W_{\pm h}$ is seen to decrease (i.e. to improve) with higher applied bias and reaches $W_{\pm h}$ = 4.8 eV/ehp at a maximal electric field of F = -5000Vcm^{-1}. Fitting the $W_{\pm h}$ values with Eq. (1.6) revealed the mobility-lifetime of holes $\mu_h \tau_h = 3.4 \times 10^{-5}$ cm^{2}V^{-1}.

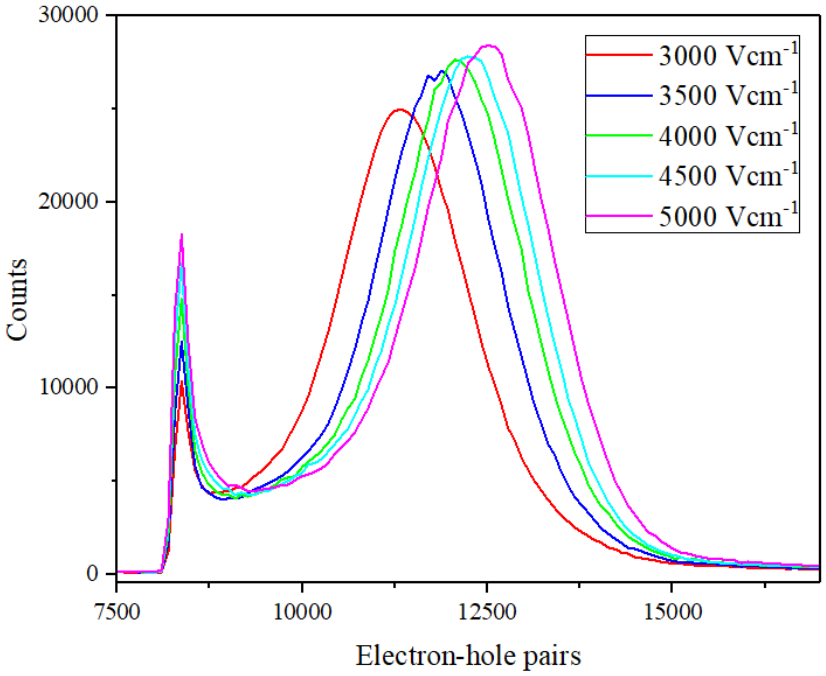

Figure 4.27. Hole pulse height spectrum obtained with different voltages applied to the solid electrode (from -3000Vcm^{-1} up to -5000Vcm^{-1}).

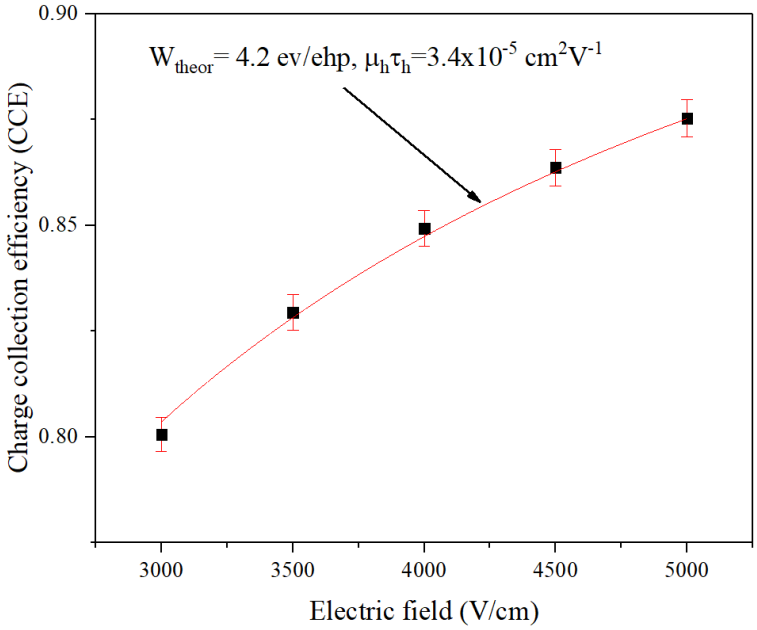

Figure 4.28. Charge collection efficiency (*CCE*) as a function of electric field for hole PHS. The black squares represent the experimental results while the red line shows the simplified Hecht fit.

4.4.3 Discussion

The independence of the electron spectral peak position on the applied electric field and a collection efficiency close to unity, indicates that almost all X-ray generated electrons transit through the sample and are successfully collected at the detector electrodes. This is not surprising, since the electron schubweg λ_e (i.e. the average distance travelled before trapping) for the smallest F = 3000Vcm^{-1} is $\lambda_e = 10.5$ cm, which is much larger than the detector thickness. In contrast, λ_h is comparable to the detector thickness and ranges from λ_h = 1.2 mm at F = 3000Vcm^{-1} to λ_h = 1.7 mm at F = 5000Vcm^{-1}. This results in an electric-field dependent charge collection efficiency ~0.85 and indicates that in any practical utilization the detector has to be placed with the cathode facing the incident radiation.

The mobility-lifetime values obtained by PHS and the mobility values calculated by TOF technique allow us to estimate the lifetime for both types of carriers as $\tau = \mu\tau/\mu$. Thus, from $\mu_h\tau_h = 3.4 \times 10^{-5}$ cm^{2}V^{-1} and μ_h=69 cm^{2}V^{-1}s^{-1}, the hole lifetime was found to be $\tau_h = 0.5\ \mu s$. Similarly, from $\mu_e\tau_e = 3.5 \times 10^{-3}$cm^{2}V^{-1} and the electron mobility μ_e=944 cm^{2}V^{-1}s^{-1}, the electron lifetime equals to $\tau_e = 3.7\ \mu s$. Overall, the obtained data on charge carriers' τ and $\mu\tau$ agree with the order of magnitude previously reported for CdZnTe, measured with alpha particles (rather than X-ray photons) [40, 38]. For example,Ruzin et al. published $\mu_e\tau_e = 2 \times 10^{-3}$ cm^{2}V^{-1}, while and Veale et al. [37] reported $\mu_e\tau_e = 1.2 \times 10^{-3}$ cm^{2}V^{-1} and $\tau_e = 1.1\ \mu s$. At the same time, the published values of the hole mobility-lifetime products were 1×10^{-5} cm^{2}V^{-1} and 5×10^{-5} cm^{2}V^{-1}, respectively. The small discrepancy in the reported values can be attributed to different CdZnTe growth conditions.

5.1. Chapter 5: Summary of the thesis and future work

5.1 Conclusion

The charge transport properties of the CdZnTe block detectors were investigated by the TOF, CELIV and PHS techniques. The electrons were found to be the faster carrier with room temperature mobility of μ_e = 939 cm^2 V^{-1}s^{-1} in sample #1 and μ_e = 944±14 cm^{2}V^{-1}s^{-1} in sample #2. The holes are more than an order of magnitude slower and at room temperature drift with mobility of μ_h = 60 cm^2 V^{-1}s^{-1} (sample #1) and μ_h = 69±3

$cm^2V^{-1}s^{-1}$ (sample #2). The temperature dependence of the carrier mobility revealed that the transport of electrons and holes are governed by different mechanisms. Electron transport is mainly controlled by charge scattering by phonons and ionized impurities, while hole transport is governed by multiple trapping into shallow centres with an activation energy of ~0.13 eV. In addition, analysis of the TOF signals revealed a spatial inhomogeneity of the electric field, due to an accumulation of a space charge in the sample #2. In order to analyze the transport properties quantitatively, a TOF theory has been extended to account for a spatially-varying electric field. As a result, the investigated CdZnTe sample #2 was found to consist of two regions with space charge densities which differ: ~2.09×10^{11} cm^{-3} and 8.15×10^{10} cm^{-3}, respectively. The width of the transition region is less than 7 μm. Near the pixelated electrode, a photo-CELIV technique detected a reservoir of trapped holes, which are quickly extracted by application of an electric field. The charge concentration in the reservoir was found to be too small to significantly affect both, electric field distribution and CdZnTe detector performance.

The PHS technique, performed with a monoenergetic x-ray source, was used to measure the mobility-lifetime products of the charge carriers, which were found to be $\mu_e\tau_e = 3.5 \times 10^{-3}$ cm^2V^{-1} and $\mu_h\tau_h = 3.4 \times 10^{-5}$ cm^2V^{-1} for electrons and holes, respectively. Such $\mu\tau$ values correspond to carrier lifetimes for electrons and holes of $\tau_e = 3.7\ \mu s$ and $\tau_h = 0.5\ \mu s$, respectively. In addition, the x-ray sensitivity of the CdZnTe block detector was investigated with PHS in terms of $W_{\pm}$. The measurements were performed over a wide range of electric fields and revealed that the $W_{\pm}$ of holes strongly depends on the applied electric field, while the $W_{\pm}$ of electrons was at a theoretical value and almost electric field independent. Such a result was related to the different schubweg of charge carriers ($\lambda_e >> \lambda_h$) and suggested that in practical utilization the incident radiation should be coming from the cathode (rather than anode) side.

5.2 Future work

The stability of CdZnTe samples and contact materials should be investigated as a part of future work to elucidate safe handling, transportation and operation conditions.

In addition, ways to restore the detector performance after undesirable heating or cooling should be investigated.

One of the current challenges of the CdZnTe studied is a relatively high level of the dark current. Reduction of the dark current is a complex problem, which requires comprehensive research of the physical processes behind it. Such research should be performed in parallel with the development of a CdZnTe blocking structure, i.e. confining CdZnTe photoconductor between two semi-insulating layers, which prevent charge injection from the electrode, while allowing the x-ray or photo-generated charge to exit.

In addition, the energy resolution of the CdZnTe block detectors needs to be established and tuned to the requirements of spectral-CT applications. For this purpose, a dedicated experimental apparatus has to be developed, which would allow to minimization of detector noise and thus allow accurate determination of the spectral full-width at half maximum, measured with various monoenergetic X-ray sources and their intensities.

References

[1] K. Zanio, R. K. Willardson, A. C. Beer and A. Treatise, Cadmium Telluride, Semiconductors and Semimetals Vol. 13, New York: Academin press , 1978.

[2] C. Kittel, Introduction to Solid State Physics, USA: John Wiley & Sons, 2005.

[3] S. Babalola O, "Surface and Bulk Defects in Cadmium Zinc Telluride and Cadmium Manganese Telluride crystals," *PhD dissertation,* 2009.

[4] P. Capper, Properties of Narrow Gap Cadmium-based Compounds, London: INSPEC, the Institution of Electrical Engineers, 1994.

[5] L. A. Kosyachenko, V. M. Sklyarchuk, O. V. Sklyarchuk and O. L. Maslyanchuk, "Band gap of CdTe and Cd0.9Zn0.1Te crystals," *Semiconductors,* vol. 45, no. 10, pp. 1273-1280, 2011.

[6] S. Del Sordo, L. Abbene, E. Caroli, A. M. Mancini, A. Zappettini and P. Ubertini, "Progress in the development of CdTe and CdZnTe semiconductor radiation detectors for astrophysical and medical applications," *Sensors,* vol. 9, no. 5, pp. 3491-3526, 2009.

[7] R. Amutha, A. Subbarayan, R. Sathyamoorthy, K. Natarajan and S. Velumani, "Conduction studies on ZnTe thin films," *Journal of New Materials for Electrochemical Systems,* vol. 10, no. 1, pp. 27-31, 2007.

[8] T. Schlesinger, J. Toney, H. Yoon, E. Lee, B. Brunett, L. Franks and R. James, "Cadmium zinc telluride and its use as a nuclear radiation detector material," *Materials Science and Engineering: R: Reports,* vol. 32, no. 4, pp. 103-189, 2001.

[9] A. Owens and A. Peacock, "Compound semiconductor radiation detectors," *Nuclear Instruments and Methods in Physics Research, Section A: Accelerators, Spectrometers, Detectors and Associated Equipment,* vol. 531, no. 1-2, pp. 18-37, 2004.

[10] M. L. Cohen and T. K. Bergstresser, "Band structures and pseudopotential form factors for fourteen semiconductors of the diamond and zinc-blende structures," *Physical Review,* vol. 141, no. 2, pp. 789-796, 1966.

[11] K. Suzuki, S. Seto, T. Sawada and K. Imai, "Carrier transport properties of HPB CdZnTe and THM CdTe:Cl," *IEEE Transactions on Nuclear Science,* vol. 49, no. 3, pp. 1287-1291, 2002.

[12] M. Prokesch and C. Szeles, "Accurate measurement of electrical bulk resistivity and surface leakage of CdZnTe radiation detector crystals," *Journal of Applied Physics,* vol. 100, no. 1, pp. 1-8, 2006.

[13] K. Suzuki, S. Seto, S. Dairaku, N. Takojima, T. Sawada and K. Imai, "Drift mobility and photoluminescence measurements on high resistivity Cd1-xZnxTe crystals grown from Te-Rich solution," *Journal of Electronic Materials,* vol. 25, no. 8, pp. 1241-1246, 1996.

[14] L. A. Kosyachenko, V. V. Motushchuk and V. M. Sklyarchuk, "Charge transport generation-recombination mechanism in Au/n-CdZnTe diodes," *Solar Energy Materials and Solar Cells,* vol. 82, no. 1-2, pp. 65-73, 2004.

[15] A. E. Bolotnikov, C. M. Hubert Chen, W. R. Cook, F. A. Harrison, I. Kuvvetli, S. M. Schindler, C. M. Stahle and B. H. Parker, "The effect of cathode bias (field effect) on the surface leakage current of CdZnTe detectors," *Nuclear Instruments and Methods in Physics Research, Section A: Accelerators, Spectrometers, Detectors and Associated Equipment,* vol. 510, no. 3, pp. 300-308, 2003.

[16] R. L. Macdonald, R. a. Linke, T. Thio, G. E. Devlin and P. Becla, "Thick plasma gratings using a local photorefractive effect in CdZnTe:In.," *Optics letters,* vol. 19, no. 24, 1994.

[17] C. K. Egan, A. Choubey and A. W. Brinkman, "Scanning tunneling microscopy and spectroscopy of the semi-insulating CdZnTe(110) surface," *Surface Science,* vol. 604, no. 19-20, pp. 1825-1831, 2010.

[18] J. L. Reno and E. D. Jones, "Growth and Optical Characterization of Strained CdZnTe/ CdTe Quantum Wells," *Journal of electronic material,* vol. 20, no. 4, pp. 2-5, 1991.

[19] M. Veale, "Charge Transport and low Temperature Phenomena in Single Crystal CdZnTe by," *PhD dissertation,* 2009.

[20] P. Rudolph, "Fundamental studies on Bridgman growth of CdTe," *Prog. Crystal Growth and Charact.,* vol. 29, pp. 275-381, 1994.

[21] F. Doty, J. Butler, J. Schetzina and K. Bowers, "Properties of CdZnTe crystals grown by a high-pressure Bridgman method," *J. Vac. Sci. Technol.,* vol. 10, pp. 1418-1422, 1992.

[22] C. Szeles and E. E. Eissler, "Current issues of high-pressure bridgman growth of semi-insulating CdZnTe," *MRS Symposium Proceeding,* vol. 487, pp. 3-12, 1998.

[23] P. Rudolph, A. Engel, I. Schentke and A. Grochocki, "Distribution and genesis of inclusions in CdTe and (Cd,Zn)Te single crystals grown by the Bridgman method and by the travelling heater method," *Journal of Crystal Growth,* vol. 147, no. 3-4, pp. 297-304, 1995.

[24] U. N. Roy, A. Burger and R. B. James, "Growth of CdZnTe crystals by the traveling heater method," *Journal of Crystal Growth,* vol. 379, pp. 57-62, 2013.

[25] C. H. Su and S. L. Lehoczky, "Growth of CdZnTe Crystals by Bridgman Technique with Controlled Overpressures of Cd," EM30 Materials and Processes Laboratory, Huntsville, AL 35812 U.S.A, 2008.

[26] H. Hermon, M. Schieber, E. Y. Lee, J. L. McChesney, M. Goorsky, T. Lam, E. Meerson, H. Yao, J. Erickson and R. B. James, "CZT detectors fabricated from horizontal and vertical Bridgman-grown crystals," *Nuclear Instruments and Methods in Physics Research, Section A: Accelerators, Spectrometers, Detectors and Associated Equipment,* vol. 458, no. 1-2, pp. 503-510, 2001.

[27] C. Szeles and M. C. Driver, "Growth and properties of semi-insulating CdZnTe for radiation detector applications," *Proceedings of SPIE - The International Society for Optical Engineering,* vol. 3446, pp. 2-9, 1998.

[28] U. N. Roy, A. Burger and R. B. James, "Growth of CdZnTe crystals by the traveling heater method," *Journal of Crystal Growth,* vol. 379, pp. 57-62, 2013.

[29] H. Chen, J. Mackenzie, R. Redden, G. Bindley, A. E. Bolotnikov, G. S. Camarda, G. Carini and R. B. James, "Characterization of Traveling Heater Method (THM)

grown Cd 0.9Zn0.1Te crystals," *IEEE Transactions on Nuclear Science,* vol. 54, no. 4, pp. 811-816, 2007.

[30] H. Chen, S. A. Awadalla, K. Iniewski, F. Harris, J. MacKenzie, T. Hasanen, W. Chen, R. Redden, G. Bindley, C. Budtz-Jorgensen, P. Luke, J. S. Lee, A. E. Bolotnikov, G. S. Camarda, Y. Cui, A. Hossain and R. B. James, "Characterization of large cadmium zinc telluride crystals grown by traveling heater method," *Journal of Applied Physics,* vol. 103, no. 1, pp. 1-5, 2008.

[31] R. A. Street, Hydrogenated Amorphous Silicon, Cambridge University Press, 1991.

[32] I. M. Blevis, D. C. Hunt and J. A. Rowlands, "Measurement of x-ray photogeneration in amorphous selenium," *Journal of Applied Physics,* vol. 85, no. 11, pp. 7958-7963, 1999.

[33] K. Hecht, "Zum Mechanismus des lichtelektrischen Primärstromes in isolierenden Kristallen," *Zeitschrift für Physik A Hadrons and Nuclei,* vol. 77, no. 3-4, pp. 235-245, 1932.

[34] O. Tousignant, L. A. Hamel, J. F. Courville, J. R. Macri, M. Mayer, M. L. McConnell and J. M. Ryan, "Transport properties and performance of CdZnTe strip detectors," *IEEE Nuclear Science Symposium & Medical Imaging Conference,* vol. 1, pp. 556-560, 1997.

[35] S. O. Kasap and C. Juhasz, "Time-of-flight drift mobility measurements on chlorine-doped amorphous selenium films," *Journal of Physics D: Applied Physics,* vol. 18, no. 4, pp. 703-720, 1985.

[36] H. Y. Cho, J. H. Lee, Y. K. Kwon, J. Y. Moon and C. S. Lee, "Measurement of the drift mobilities and the mobility-lifetime products of charge carriers in a CdZnTe crystal by using a transient pulse technique," *Journal of Instrumentation,* vol. 6, no. 1, 2011.

[37] M. C. Veale, P. J. Sellin, A. Lohstroh, A. W. Davies, J. Parkin and P. Seller, "X-ray spectroscopy and charge transport properties of CdZnTe grown by the vertical Bridgman method," *Nuclear Instruments and Methods in Physics Research,*

Section A: Accelerators, Spectrometers, Detectors and Associated Equipment, vol. 576, no. 1, pp. 90-94, 2007.

[38] A. Ruzin and Y. Nemirovsky, "Methodology for evaluation of mobility-lifetime product by spectroscopy measurements in CdZnTe spectrometers," *Journal of Applied Physics,* vol. 82, no. 1997, pp. 4166-4171, 1997.

[39] H. R. Zulliger and D. W. Aitken, "Charge Collection Efficiencies for Lithium-Drifted Silicon and Germanium Detectors in the X-Ray Energy Region," *IEEE Transactions on Nuclear Science,* vol. 15, no. 1, pp. 466-474, 1968.

[40] N. Auricchio, L. Marchini, E. Caroli, A. Zappettini, L. Abbene and V. Honkimaki, "Charge transport properties in CdZnTe detectors grown by the vertical Bridgman technique," *Journal of Applied Physics,* vol. 110, no. 12, pp. 1-8, 2011.

[41] K. Suzuki, S. Seto, A. Iwata and M. Bingo, "Transport Properties of Undoped Cd0.9Zn0.1Te Grown by High Pressure Bridgman Technique," *Journal ofElectronic Materials,* vol. 29, no. 6, pp. 704-707, 2000.

[42] K. Suzuki, T. Sawada and S. Seto, "Electric field inhomogeneity in ohmic-type CdTe detectors measured by time-of-flight technique," *Physica Status Solidi (C),* vol. 13, no. 7-9, pp. 656-660, 2016.

[43] K. Suzuki, T. Sawada and K. Imai, "Effect of DC bias field on the time-of-flight current waveforms of CdTe and CdZnTe detectors," *IEEE Transactions on Nuclear Science,* vol. 58, no. 4, pp. 1958-1963, 2011.

[44] G. Zentai, "Photoconductor-based (direct) large-area x-ray imagers," *Journal of Society for Information Display,* vol. 17, no. 6, pp. 543-550, 2009.

[45] J. S. Iwanczyk, Radiation Detectors for Medical Imaging, CRC Press, 2015.

[46] J. Beutel and H. L. V. M. R. L. Kundel, Handbook of Medical Imaging Volume 1. Physics and Psychophysics, Bellingham: SPIE, 2000.

[47] B. Redus, "Efficiency of Amptek XR-100T-CdTe and -CZT Detectors," Amptek Inc., 2002.

[48] C. A. Klein, "Bandgap dependence and related features of radiation ionization energies in semiconductors," *Journal of Applied Physics,* vol. 39, no. 4, pp. 2029-2038, 1968.

[49] S. Kasap, J. Frey, G. Belev, O. Tousignant, H. Mani, J. Greenspan, L. Laperriere, O. Bubon, A. Reznik, G. DeCrescenzo, K. Karim and J. Rowlands, "Amorphous and Polycrystalline Photoconductors for Direct Conversion Flat Panel X-Ray Image Sensors," *Sensors ,* vol. 11, no. 5, pp. 5112-5157, 2011.

[50] H. O. Anger, "Scintillation camera," *Review of Scientific Instruments,* vol. 29, no. 1, pp. 27-33, 1958.

[51] T. E. Schlesinger, B. Brunett, H. Yao, J. M. Vanscyoc, R. B. James, K. Chattopadhyay, X.-Y. MA, A. Burger, N. Giles, U. El-Hanany, A. Shahar and A. Tsigelman, "Large volume imaging arrays for gamma-ray spectroscopy," *Journal of Electronic Materials,* no. 6, pp. 864-878, 1999.

[52] T. Narita, P. F. Bloser, J. E. Grindlay, J. A. Jenkins and H. W. Yao, "Development of IMARAD CZT detectors with PIN contacts," *Proceedings of SPIE - The International Society for Optical Engineering,* vol. 3768, pp. 55-65, 1999.

[53] J. F. Butler and C. L. Lingren, "CdZnTe solid-state gamma camera," *IEEE Transactions on Nuclear Science,* vol. 45, pp. 359-363, 1998.

[54] Y. Eisen, I. Mardor, A. Shor, Z. Baum, D. Bar, G. Feldman, H. Cohen, E. Issac, R. Haham-Zada, S. Blitz, Y. Cohen, B. Glick, R. Falk, S. Roudebush and I. Blevis, "NUCAM3 - A gamma camera based on segmented monolithic CdZnTe detectors," *IEEE Transactions on Nuclear Science,* vol. 49, no. 4, pp. 1728-1732, 2002.

[55] I. M. Blevis, M. K. O'Connor, Z. Keidar, A. Pansky, H. Altman and J. W. Hugg, "CZT gamma camera for scintimammography," *Physica Medica,* vol. 21, pp. 56-59, 2006.

[56] B. Mueller, M. K. O'Connor, I. Blevis, R. Smith, D. A. Collins and S. W. Phillips, "Evaluation of a small cadmium zinc telluride detector for scintimammography.," *Journal of nuclear medicine : official publication, Society of Nuclear Medicine,* vol. 44, no. 4, pp. 602-609, 2003.

[57] M. Bocher, I. M. Blevis, L. Tsukerman, Y. Shrem, G. Kovalski and L. Volokh, "Bocher, M., Blevis, I. M., Tsukerman, L., Shrem, Y., Kovalski, G., & Volokh, L. (2010). A fast cardiac gamma camera with dynamic SPECT capabilities: Design, system validation and future potential. European Journal of Nuclear Medicine and Molecular Imaging," *European Journal of Nuclear Medicine and Molecular Imaging,* vol. 37, no. 10, pp. 1887-1902, 2010.

[58] J. Kočka, O. Klíma, G. Juška, M. Hoheisel and R. Plättner, "SCLC transients in a-Si:H - New features and possibilities," *Journal of Non-Crystalline Solids,* Vols. 137-138, no. 1, pp. 427-430, 1991.

[59] G. Juška, A. Matulionis and J. Viščakas, "Hole Generation in Amorphous Selenium," *Physica status solidi a,* vol. 4, no. 3, pp. 787-796, 1971.

[60] Š. Uxa, E. Belas, R. Grill, P. Praus and R. B. James, "Determination of Electric-Field Profile in CdTe and CdZnTe Detectors Using Transient-Current Technique," *IEEE Transactions on Nuclear Science,* vol. 59, no. 5, pp. 2402-2408, 2012.

[61] K. Suzuki, T. Sawada and S. Seto, "Temperature-Dependent measurements of time-of-flight current waveforms in Schottky CdTe detectors," *IEEE Transactions on Nuclear Science,* vol. 60, no. 4, pp. 2840-2844, 2013.

[62] M. Abramowitz and I. A. Stegun, Handbook of Mathematical Functions: with Formulas, Graphs, and Mathematical Tables (Dover Books on Mathematics), New York: Dover Publications, 1972.

[63] S. Kalashnikov and L. Bonch-Bruevich, The Physics of Semiconductors, Moscow: Main Editorial Board for Physical and Mathematical Literature, 1977.

[64] S. S. Li, "Scattering Mechanisms and Carrier Mobilities in Semiconductors," in *Semiconductor Physical Electronics*, Springer US, 1993, pp. 183-211.

[65] S. Li, "Scattering Mechanisms and Carrier Mobilities in Semiconductors," in *Semiconductor Physical Electronics*, Springer US, 1993, pp. 183-211.

[66] I. Blevis, "Method and apparatus for reducing polarization within an imaging device". USA Patent US7312458 B2, 25 12 2007.

[67] G. Juška, K. Arlauskas, M. Viliūnas and J. Kočka, "Extraction Current Transients: New Method of Study of Charge Transport in Microcrystalline Silicon," *Phys. Rev. Lett,* vol. 84, no. 21, pp. 4946-4949, 2000.

[68] A. Pivrikas, N. S. Sariciftci, G. Juška and R. Österbacka, "A review of charge transport and recombination in polymer/fullerene organic solar cells," *Progress in Photovoltaics: Research and Applications,* vol. 15, no. 8, p. 677–696, 2007.

[69] I. Blevis, "Method and apparatus for reducing polarization within an imaging device". USA Patent US 7312458 B2, 25 Dec 2007.

[70] D. E. Cullen, M. H. Chen, J. H. Hubbell, S. T. Perkins, E. F. Plechaty, J. A. Rathkopf and J. H. Schfield, Tables and Graphs of Photon-interaction Cross Sections from 10eV to 100 GeV Derived from the LLNL Evaluated Photon Data Library (EPDL), Lawrence Livermore National Laboratory, 1989.

[71] V. Boothman, A. Alruhaili, V. Perumal, P. Sellin, A. Lohstroh, K. Sawhney and S. Kachanov, "Charge transport optimization in CZT ring-drift detectors," *Journal of Physics D: Applied Physics,* vol. 48, no. 48, 2015.

Appendix A: Solution of the Poisson equation

In this appendix, we detail the solving of Poisson equation for the two-region crystals using the space charge density written in (4.10):

$$\Delta\varphi(x) = \frac{\rho(x)}{\varepsilon\varepsilon_0} \tag{A.1}$$

$$\rho(x) = q\left(N_1 + N_2 \frac{1}{1+e^{2k(x-x_0)}} \right) \tag{A.2}$$

Let's define $\theta = \frac{q}{\varepsilon\varepsilon_0}$.

Eq. (A.1) is the inhomogeneous differential equation of a second order. To solve it, Lagrange's variation of parameters method was used. The solution of homogeneous equation where constants are substituted by the coordinate functions (due to variation of parameters method) is:

$$\varphi(x) = C_1(x)x + C_2(x) \tag{A.3}$$

The $C_1(x)$ and $C_2(x)$ can be obtained as a solution of the following system:

$$\begin{cases} xC_1'(x) + C_2'(x) = 0 \\ C_1'(x) = \theta\left(N_1 + \frac{N_2}{1+e^{2k(x-x_0)}} \right) \end{cases} \tag{A.4}$$

Prime symbol from now on means the first derivative of any function with respect to coordinate. From second equation of system (A.4):

$$C_1(x) = \theta\int\left(N_1 + \frac{N_2}{1+e^{2k(x-x_0)}} \right)dx = \theta N_1 x + C_1^* + N_2\theta\int\frac{1}{1+e^{2k(x-x_0)}}dx \tag{A.5}$$

Here C_1^* is the integration constant. Using the substitution:

$$t = e^{2k(x-x_0)} \tag{A.6}$$

the integral in the right part of (A.5) could be calculated and (A.5) can be written as:

$$C_1(x) = \theta(N_1 + N_2)x - \frac{\theta N_2}{2k}\ln\left(1+e^{2k(x-x_0)}\right) + C_1^* \tag{A.7}$$

$C_2(x)$ can be obtained from the rewritten first equation of (A.4):

$$C_2'(x) = -xC_1'(x) \tag{A.8}$$

Using eq. (A.7):

$$C_1'(x) = \theta(N_1 + N_2) - \theta N_2 \frac{e^{2k(x-x_0)}}{1+e^{2k(x-x_0)}} \quad \text{(A.9)}$$

and from (A.8):

$$C_2(x) = -\int x\theta(N_1 + N_2)dx + \theta N_2 \int x \frac{e^{2k(x-x_0)}}{1+e^{2k(x-x_0)}}dx \quad \text{(A.10)}$$

Using the substitution shown in (A.6):

$$C_2(x) = -\frac{1}{2}x^2(N_1 + N_2) + \frac{\theta N_2}{2k} x \ln\left(1+e^{2k(x-x_0)}\right) + \\ + \frac{\theta N_2}{4k^2}\mathrm{Li}_2\left(-e^{2k(x-x_0)}\right) + C_2^* \quad \text{(A.11)}$$

C_2^* is the integration constant. $Li_\alpha(x)$ from now on is a polylogarithmic function of order α.

The solution of the Poisson equation (A.1) could be written as:

$$\varphi(x) = \frac{1}{2}\theta(N_1 + N_2)x^2 + \frac{1}{4k^2}\theta N_2 \mathrm{Li}_2\left(-e^{2k(x-x_0)}\right) + C_1^* x + C_2^* \quad \text{..... (A.12)}$$

The integration constants could be found from the boundary conditions:

$$\begin{cases} \varphi(0) = \varphi_0 \\ \varphi(d) = 0 \end{cases} \quad \text{(A.13)}$$

From the first equation of (A.13):

$$C_2^* = \varphi_0 - \frac{\theta N_2}{4k^2}\mathrm{Li}_2\left(-e^{-2kx_0}\right) \quad \text{(A.14)}$$

From the second equation of (A.13):

$$C_1^* = \frac{1}{d}\left\{\frac{\theta N_2}{4k^2}\left[\mathrm{Li}_2\left(-e^{-2kx_0}\right) - \mathrm{Li}_2\left(-e^{2k(d-x_0)}\right)\right] - \frac{1}{2}\theta d^2(N_1 + N_2) - \varphi_0\right\}$$

(A.15)

Taking into account (A.14) and (A.15), the solution of the Poisson equation is:

$$\varphi(x) = -\frac{1}{4dk^2}\left\{(d-x)\zeta(x) + N_2\theta\xi(x)\right\}, \quad \text{(A.16)}$$

where

$$\zeta(x) = 2k^2\left(\theta d\left(N_1 + N_2\right)x - 2\varphi_0\right) + \theta N_2 \,\mathrm{Li}_2\left(-e^{-2kx_0}\right)$$
$$\xi(x) = x\,\mathrm{Li}_2\left(-e^{2k(d-x_0)}\right) - d\,\mathrm{Li}_2\left(-e^{2k(x-x_0)}\right) \tag{A.17}$$

This theory could be expanded to the situation of M regions. In this case the space charge density distribution can be written in the following form:

$$\rho(x) = q\left(N_1 + \sum_{i=2}^{M} \frac{N_i}{1 + e^{2k_i(x-x_{0i})}}\right) \tag{A.18}$$

Index *i* represents the region number, x_{0i} corresponds to the center of transition zone in the *i*th region. Using the approach described above in this appendix, the electric potential in the M-regions crystal will be:

$$\varphi_M(x) = \frac{1}{4d}\left\{(d-x)\zeta_M(x) + \theta\xi_M(x)\right\}$$
$$\zeta_M = 2\left(2\varphi_0 - \theta dx\sum_{i=1}^{M} N_i\right) - \theta\sum_{i=2}^{M}\frac{N_i}{k_i^2}\mathrm{Li}_2\left(-e^{-2k_i x_{0i}}\right) \tag{A.19}$$
$$\xi_M = d\sum_{i=2}^{M}\frac{N_i}{k_i^2}\mathrm{Li}_2\left(-e^{-2k_i(x-x_{0i})}\right) - x\sum_{i=2}^{M}\frac{N_i}{k_i^2}\mathrm{Li}_2\left(-e^{2k_i(d-x_{0i})}\right)$$

Appendix B: Calculation of the intrinsic electric field

In this appendix, we detail the calculation of the electric field in the two-region crystal with an inhomogeneous distribution of space charge density. The electric field **F** could be calculated as:

$$\mathbf{F}(x) = -\nabla\varphi(x). \tag{B.1}$$

where φ is an electric potential. Using the (A.16) it could be written:

$$\frac{\partial}{\partial x}\varphi(x) = -\frac{1}{4dk^2}\left\{-\zeta(x) + (d-x)\zeta'(x) + \theta N_2 \xi'(x)\right\}. \tag{B.2}$$

Let's calculate the first derivatives of functions $\zeta(x)$ and $\xi(x)$ with respect to coordinate:

$$\zeta'(x) = 2k^2\theta d\,(N_1 + N_2) \tag{B.3}$$

$$\xi'(x) = \mathrm{Li}_2\left(-e^{2k(d-x_0)}\right) + 2kd\ln\left(1 + e^{2k(x-x_0)}\right) \tag{B.4}$$

Using eq. (B.2) – (B.4) the intrinsic electric field distribution could be calculated:

$$F(x) = \frac{1}{4dk^2}\left\{2k\eta(x) + \theta N_2\left[\mathrm{Li}_2\left(-e^{2k(d-x_0)}\right) - \mathrm{Li}_2\left(-e^{2kx_0}\right)\right]\right\}, \tag{B.5}$$

where

$$\eta(x) = k\left(2\varphi_0 + \theta(N_1 + N_2)d\,(d-2x)\right) + \theta d N_2 \ln\left(1 + e^{2k(x-x_0)}\right) \tag{B.6}$$

In the case of M-region crystal, using the equations (B.1, A.19) the internal electric field takes the form of:

$$F_M(x) = \frac{1}{4d}\left\{2\eta_M(x) + \theta\sum_{i=2}^{M}\frac{N_i}{k_i^2}\left[\mathrm{Li}_2\left(-e^{2k_i(d-x_{0i})}\right) - \mathrm{Li}_2\left(-e^{-2k_i x_{0i}}\right)\right]\right\} \tag{B.7}$$

where:

$$\eta_M(x) = 2\varphi_0 + \theta d\,(d-x)\sum_{i=1}^{M} N_i + \theta d\sum_{i=2}^{M}\frac{N_i}{k_i}\ln\left(1 + e^{2k_i(x-x_{0i})}\right) \tag{B.8}$$

Here, i and x_{0i} represent the number of region and the center of the transition zone respectively.